Titre: Title:	Performance of Background Field Removal and Dipole Inversion Methods to Reconstruct Brain Quantitative Susceptibility Mapping (QSM) Data Acquired in Neonatal Asphyxia
Auteur: Author:	Daniel Ridani
Date:	2023
Type:	Mémoire ou thèse / Dissertation or Thesis
Référence: Citation:	Ridani, D. (2023). Performance of Background Field Removal and Dipole Inversion Methods to Reconstruct Brain Quantitative Susceptibility Mapping (QSM) Data Acquired in Neonatal Asphyxia [Mémoire de maîtrise, Polytechnique Montréal]. PolyPublie. https://publications.polymtl.ca/10828/

URL de PolyPublie: PolyPublie URL:	https://publications.polymtl.ca/10828/
Directeurs de recherche: Advisors:	Benjamin De Leener, & Mathieu Dehaes
Programme: Program:	Génie biomédical

POLYTECHNIQUE MONTRÉAL

affiliée à l'Université de Montréal

Performance of Background Field Removal and Dipole Inversion Methods to Reconstruct Brain Quantitative Susceptibility Mapping (QSM) Data Acquired in Neonatal Asphyxia

DANIEL RIDANI

Institut de génie biomédical

Mémoire présenté en vue de l'obtention du diplôme de *Maitrise ès sciences appliquées*

Génie biomédical

Février 2023

POLYTECHNIQUE MONTRÉAL

affiliée à l'Université de Montréal

Ce mémoire intitulé :

Performance of Background Field Removal and Dipole Inversion Methods to Reconstruct Brain Quantitative Susceptibility Mapping (QSM) Data Acquired in Neonatal Asphyxia

présenté par **Daniel RIDANI**

en vue de l'obtention du diplôme de *Maitrise ès sciences appliquées*

a été dûment accepté par le jury d'examen constitué de :

Samuel KADOURY, président
Benjamin DE LEENER, membre et directeur de recherche
Mathieu DEHAES, membre et codirecteur de recherche
Eva ALONSO ORTIZ, membre

DEDICATION

For my family who have always supported me.
Pour ma famille qui m'a toujours soutenu.

ACKNOWLEDGEMENTS

I want to express my sincere gratitude to my master's supervisor, Benjamin De Leener, for his invaluable guidance and support throughout my master's degree. His expertise and insights were instrumental in helping me to achieve my goals.

I would also like to thank my co-supervisor, Mathieu Dehaes, for his valuable contribution and support throughout my research. His expertise and guidance are greatly appreciated.

I am grateful to the members of the jury Samuel Kadoury and Eva Alonso Ortiz for agreeing to be part of the jury of my defense.

I would like to thank my colleagues in NeuroPoly and CHU Saint Justine, Andjela, Colline, Erjun, Antoine, and Noée for their support and friendship during my time in the laboratory. I learned much from them and enjoyed working with them.

I would also like to thank my father Raouf, my mother Sania, and my sister Jana for their unwavering support and encouragement throughout my studies. Their love and support meant the world for me.

Finally, I would also like to extend special thanks to my friend Raed. His presence on my side has been invaluable to me, and I am grateful to have him in my life.

RÉSUMÉ

Largement utilisée dans le cerveau humain, l'imagerie par résonance magnétique (IRM) est une technique d'imagerie médicale non invasive à haute résolution qui utilise des rayonnements non ionisants pour produire un bon contraste des tissus mous et des données potentiellement utiles. La susceptibilité magnétique des tissus, qui peut refléter la composition du tissu, a un impact sur le signal en IRM. Des techniques de cartographie de susceptibilité quantitative (QSM) ont récemment été utilisées pour évaluer la susceptibilité magnétique, un attribut physique de la matière, dans les tissus biologiques. En utilisant des images de phase IRM qui sont enregistrées en même temps que des images de magnitude conventionnelles pour reconstruire la distribution spatiale de susceptibilité. Par conséquent, QSM détermine la distribution de susceptibilité en résolvant le problème inverse mal poser consistant à obtenir la distribution de susceptibilité à partir de la perturbation de champ dans les données de phase. Pour résoudre ce problème inverse, plusieurs étapes de prétraitement doivent avoir lieu, comprenant trois étapes principales : du déballage de phase au déballage de l'image de phase puisque les données de phase du scanner sont limitées à la plage [-π, π]. Toute phase enregistrée en dehors de cette plage y sera repliée, produisant un enroulement de phase, qui est un saut dans les données de phase, puis l'élimination des perturbations de champ magnétique de fond causées en dehors du volume d'intérêt. Enfin, l'inversion dipolaire pour estimer la susceptibilité locale. Il existe de nombreuses utilisations du QSM, y compris la susceptibilité magnétique peut être utilisée pour diagnostiquer et surveiller de nombreuses maladies, notamment la maladie de Parkinson, la maladie de Huntington, la sclérose en plaques et l'encéphalopathie hypoxique-ischémique (HIE), ainsi que la myélinisation, les microhémorragies et le métabolisme du fer. Cette thèse était spécifiquement dédiée aux nouveau-nés diagnostiqués avec HIE, qui es une condition médicale qui provoque un manque d'oxygène dans le cerveau du nourrisson, ce qui peut entrainer des résultats neurodéveloppement aux indésirables. Ayant un taux de mortalité élevé, HIE a été un sujet d'intérêt pour de nombreux chercheurs qui tenet de trouver un biomarqueur précoce pour détecter les lésions cérébrales.

Les objectifs de cette thèse sont les suivants : développer un socle de physique de l'IRM avec un focus et des séquences IRM multi-échos ; passer en revue la littérature de QSM pour chaque étape de pré-traitement ; expliquer le danger de l'HIE pour les nouveau-nés, ; comparer différents pipelines de reconstruction d'images pour évaluer l'oxygénation cérébrale, à l'aide de QSM, pour

les nouveau-nés diagnostiqués avec HIE et ayant subi une hypothermie thérapeutique qui consiste à refroidir les patients pendant les 72 premières heures de vie. La comparaison sera effectuée en choisissant les algorithmes les plus utilisés de suppression du champ de fond et d'inversion dipolaire et en faisant différentes combinaisons à partir d'eux, puis en les comparant à l'aide de différentes métriques. Les valeurs de susceptibilité des niveaux d'oxygénation seront également extraites pour les comparer.

Les résultats de ce projet nous amènent à croire que le choix de l'inversion dipolaire et de la suppression du champ de fond affecte les valeurs de susceptibilité et d'oxygénation. En conséquence, pour garantir des résultats optimaux, les stratégies de traitement QSM doivent être soigneusement sélectionnées en fonction de la question d'intérêt: soit un intérêt pour l'évaluation quantitative (valeurs d'oxygénation et de susceptibilité) ou l'évaluation qualitative.

ABSTRACT

Magnetic resonance imaging (MRI), widely employed in the human brain, is a high-resolution, non-invasive medical imaging technique that uses non-ionizing radiation to produce good soft tissue contrast and potentially meaningful data. The magnetic susceptibility of tissues, which may reflect the tissue's composition, affects MRI signals. Quantitative susceptibility mapping (QSM) techniques have recently been used to assess magnetic susceptibility, a physical attribute of matter, within biological tissues, by utilizing MRI phase images recorded concurrently with conventional magnitude images to rebuild the spatial susceptibility distribution. QSM determines the susceptibility distribution by resolving the ill-posed inverse problem of obtaining the susceptibility distribution from the field perturbation in the phase data. To solve this inverse problem, three major preprocessing steps should take place: phase unwrapping to unwrap the phase image since the scanner's phase data is restricted to the range $[-\pi,\pi]$. Any phase value recorded outside this range will be aliased back into it, producing a phase wrap, which is a jump in the phase data, followed by the elimination of background magnetic field disturbances caused outside the volume of interest. Finally, dipole inversion to estimate local susceptibility. There are numerous uses of QSM, including magnetic susceptibility, which can be used to diagnose and monitor illnesses, including Parkinson's, Huntington's, Multiple Sclerosis, and hypoxic-ischemic encephalopathy (HIE), as well as myelination, microbleeds, and iron metabolism. This thesis is specifically dedicated to neonates diagnosed with HIE, which is a medical condition that causes a lack of oxygen in the infant's brain which can lead to adverse neurodevelopmental outcomes. Having a high mortality rate, HIE has been a topic of interest for many researchers that are trying to find an early biomarker to detect brain injury.

The goals of this thesis are as follows: to develop a foundation of MRI physics with a focus and multi-echo MRI sequences; to review the literature of QSM for each pre-processing step; to explain the danger of HIE for neonates; compare different image reconstruction pipelines to assess brain oxygenation, using QSM, for neonates diagnosed with HIE who underwent therapeutic hypothermia that consists in cooling patients during the first 72 h of age. The comparison will be performed by choosing the most used background field removal and dipole inversion algorithms, making different combinations out of them, and then comparing them using different metrics. The susceptibility values and oxygenation levels were also extracted for comparison.

The findings of this project lead us to believe that the choice of dipole inversion and background field removal can affect susceptibility and oxygenation values. Accordingly, to ensure optimal results, QSM processing strategies should be carefully selected based on the questions of interest: either interest in quantitative assessment (oxygenation and susceptibility values) or qualitative assessment.

TABLE OF CONTENTS

LIST OF TABLES

LIST OF FIGURES

LIST OF SYMBOLS AND ABBREVIATIONS

AD	Alzheimer's disease
BET	Brain extraction tool
bSSFP	Balanced Steady-State Free Precession
CSvO2	Cerebral venous oxygen saturation
CSF	Cerebrospinal fluid
CT	Computed tomography
CL	Continuous Laplacian
COSMOS	Computational solution for this multi-orientation scheme
DL	Discrete Laplacian
FID	Free induction decay
GM	Gray matter
GRE	Gradient echo
HIE	Hypoxic-ischemic encephalopathy
HD	Huntington's disease
HCT	Hematocrit
ISMV	Iterative spherical mean value method
LBV	Laplacian boundary value

MRI	Magnetic resonance imaging
MR	Magnetic resonance
MEDI	Morphology Enabled Dipole Inversion
NIRS	Near-infrared resonance spectroscopy
NDI	Nonlinear dipole inversion
PDF	Projection into dipole
PD	Parkinson's disease
PROPELLER	Periodically Rotated Overlapping ParallEL Lines with Enhanced Reconstruction
QSM	Quantitative susceptibility mapping
QG	Quality guided
RF	Radiofrequency
ROI	Region of interest
RESHARP	Regularization enabled sophisticated harmonic artefact reduction for phase data
RTS	Rapid two-step dipole
RG	Region-growing
SNR	Signal to noise ratio
SENSE	Sensitivity encoding
SWI	Susceptibility weighted imaging

SN	Substantia nigra
SHARP	Sophisticated harmonic artefact reduction for phase data
STAGE	Strategically Acquired Gradient Echo
TR	Repetition time
TE	Echo time
TSVD	Truncated Singular Value Decomposition
TKD	Truncated k-space Division
TIKH	Tikhonov regularization
TV	Total variation
UMPIRE	Unwrapping multi-echo phase images with irregular echo spacings
VSHARP	Variable kernel sophisticated harmonic artefact reduction for phase data
WM	White matter
2D	Two-dimensional
3D	Three-dimensional

LIST OF APPENDICES

CHAPTER 1 INTRODUCTION

1.1 Motivations and objectives

Magnetic resonance imaging (MRI), and mainly quantitative susceptibility mapping (QSM), which uses the image phase signal from gradient echo to determine the local tissue magnetic susceptibility value [1], is an emerging MRI technique that has gained considerable attention among the community to develop it over a wide range of reconstruction algorithms. QSM makes it possible to quantify brain oxygenation and therefore offers a relevant measure to assess brain integrity and response to therapy in newborns with hypoxic-ischemic encephalopathy (HIE) who undergo hypothermia [2]. Its potential for quantitative blood oxygenation measurements has been shown in several studies, and it holds great promise [11,12].

Neonatal hypoxic-ischemic encephalopathy (HIE) or birth asphyxia is a clinical syndrome of neurological dysfunction that occurs in 1.5 cases per 1000 live births [3]. The World Health Organization estimates that 8% of deaths in children under the age of five are due to HIE at birth [4]. Currently, hypothermia therapy is the only treatment that has shown a decrease in mortality, and consists of cooling patients during the first 72 h of age [5]. Although therapeutic hypothermia improves survival rates and reduces severe neurodevelopmental disability, a significant number of neonates still suffer from brain injury and adverse neurodevelopmental outcomes [6]. Hence, early markers of impaired cerebral venous oxygen saturation (CSvO2), which is the amount of leftover oxygen in the veins after oxygen delivery and extraction by the brain, may help to detect brain injury on post-therapy MRI and improve long-term outcomes. While normal values are between 65-75%, elevated values of CSvO2 suggest serious brain injury [7]. The two available methods to measure CSvO2 are invasive, such as inserting an internal jugular vein catheter and non-invasive methods, such as near-infrared resonance spectroscopy (NIRS) have been shown to have poor sensitivity at low CSvO2 [8].

However, the current QSM image reconstruction methods have not been developed for the developing brain, which may affect the quantification of oxygenation levels, since the oxygenation levels are directly related to the susceptibility values, therefore, an inaccurate estimation of the susceptibility values will affect the oxygenation levels . Additionally, QSM for neonatal imaging

may require a more complex reconstruction process due to the smaller brain structure and shorter acquisition time of the newborn can affect images quality. In this thesis, I compared different QSM reconstruction algorithms to quantify the level of cerebral venous oxygen saturation in patients who underwent therapeutic hypothermia for HIE.

1.2 Thesis Outline

The remainder of this thesis is organized as follows:

Chapter 2 presents a literature review, background information on the basic principles of MRI and the necessary concepts for understanding the work described in this thesis. The interaction of magnetic fields with nuclear spins and the use of radiofrequency fields and linear gradient fields in MRI, relaxation, and signal detection are discussed in this chapter. Multi-echo gradient echo sequences are discussed in detail in this chapter as they serve as the foundation for gathering experimental data for QSM. In addition, this chapter covers the fundamentals of QSM and its relationship with phase data, as well as the used pipeline to reconstruct the QSM image, which contains several steps, such as phase unwrapping, background removal, and dipole inversion, which are explained in detail for each step. This work also presents multi-orientation QSM, also known as computational solution for this multi-orientation scheme (COSMOS). Finally, this chapter closes with an explanation of QSM for neonates.

Chapter 3 describes the scientific methodology that has led to the submission of the article related to this project.

Chapter 4 presents the submitted article, titled: Development and comparison of image reconstruction pipelines to assess brain oxygenation in neonatal asphyxia using quantitative susceptibility mapping (QSM)

Chapter 5 discusses the results of this project as well as its limitations.

Chapter 6 presents the conclusions of this project, and future work planned to improve the robustness of QSM and overcome limitations.

CHAPTER 2 LITERATURE REVIEW

2.1 Magnetic resonance physics

Magnetic resonance imaging is a medical imaging technique used in radiology that produces images of an object's internal physical and chemical characteristics by measuring the magnetic resonance signal induced by the interaction between the external magnetic field and nuclear spins [9]. Recently, MRI has gained popularity as a non-invasive imaging tool for a wide range of applications. Moreover, MRI provides better soft-tissue contrast [10] than X-ray and CT scan. All the excited spins contribute to a time signal that is proportional to the total magnetization. Although the best way to describe the functionality of an MRI is by quantum physics, for a large group of spins, an analogy of classical physics will help interpret the different phenomena easily. Therefore, an efficient introduction to MR basic physics will be presented in this section.

If we consider a nucleus as a charged sphere spinning about itself, this nucleus will create a magnetic moment because it has mass and charge. Similarly, elementary particles such as protons, electrons and neutrons possess intrinsic angular momentum called spin angular momentum or simply "Spin". Spin can only be observed in atoms that have an odd number of protons or electrons (such as hydrogen in water, which is the most abundant atom in the majority of biological soft tissues), since nucleons tend to group in a way in which opposite angular momentum is canceled and creates a zero momentum [11]. The spin angular momentum can be described by vector S= [S_x, S_y, S_z]. In quantum mechanics the spin angular momentum is related to the spin magnetic moment μ by the following formula: [10]

$$\mu = \gamma S \tag{2.1}$$

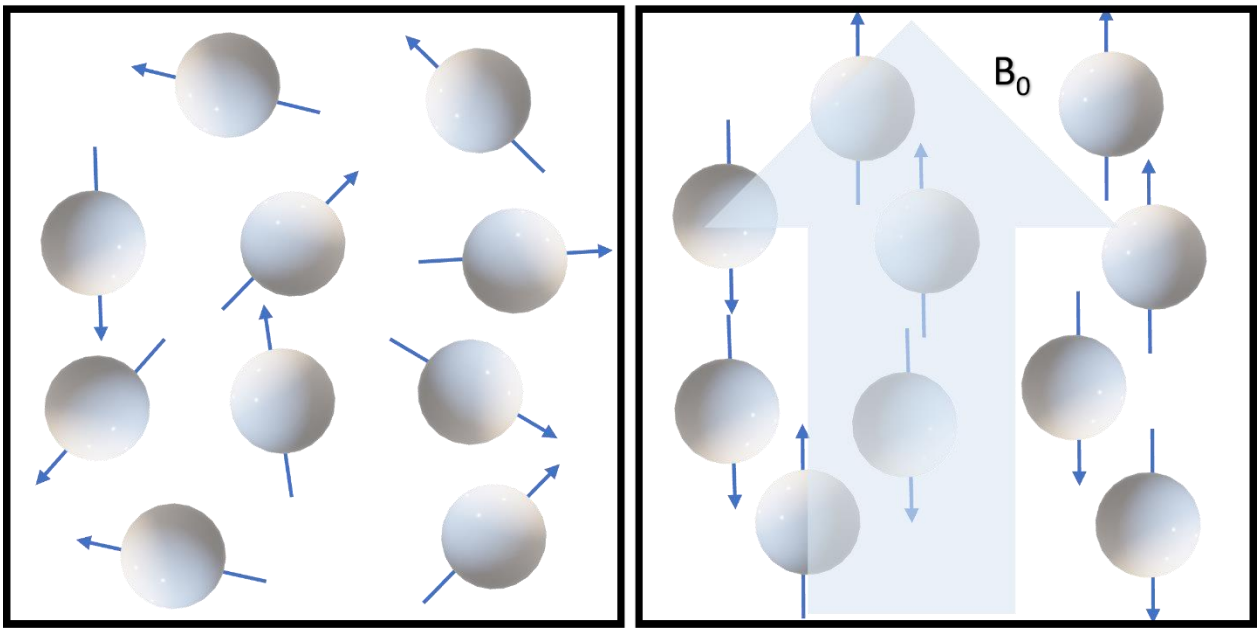

Figure 2-1: Alignment of spins with and without the presence of external magnetic field.

Where, γ is the gyromagnetic ratio of the spin defined by $\gamma = g\frac{q}{2m}$, where q is the charge of the particle, m is the mass, and g is called the g-factor, which is measured experimentally.

When a strong external magnetic field B_0 is applied, spins tend to align with B_0 generating a net magnetization M_0. Net magnetization can be defined as:

$$M_0 = \frac{N\gamma^2\hbar^2 s(s+1)}{3KT} B_0 \tag{2.2}$$

Where N is the total spin population, $\hbar$ is the Plank constant $\hbar = 1.05 \times 10^{-34}\, J.s$, s is the spin, K is the Boltzmann constant K=$1.38 \times 10^{-23}\frac{J}{K}$, and T is the temperature. As shown in Figure 2-1, when there is no external magnetic field, the spins are randomly directed, but when an external magnetic field B_0 is applied, the spins align themselves along the field in a parallel or anti-parallel state. In reality, this phenomenon can be explained by quantum theory as discrete levels of energy. In general, in the hydrogen atom case, the spin is ½, so we have two discrete energy levels defined as low energy level when the spins are parallel to B_0 and high energy level when the spins are anti-parallel to B_0. The distribution of spins between energy levels can be described by Boltzmann

statistics. Thus, the probability of finding a spin in an energy level is proportional to the Boltzmann distribution:

$$P(N) \propto e^{-\frac{E}{KT}} \tag{2.3}$$

Where E is the energy level, T is the temperature, and k is the Boltzmann constant.

Using the Boltzmann distribution, we can deduce the ratio between the parallel and anti-parallel spins:

$$\frac{N_+}{N_-} = \exp\left(\frac{\gamma\hbar B_0}{KT}\right) \tag{2.4}$$

At thermal equilibrium, the magnetization M point in the direction of B_0. If it is tipped away from the axis of B_0, M will start to precess, resulting from the torque imposed by the magnetic field given by:

$$\frac{dM}{dt} = M \times \gamma B \tag{2.5}$$

This precession has a certain angular frequency called Larmor frequency (w):

$$\omega_0 = \gamma B_0 \tag{2.6}$$

The quantum mechanics spin and the classical physics spin are directly related through the precession of spin ½. In other words, when an energy of frequency ω_0 is applied, the spin ½ particles transition between the two different states.

2.2 Spin excitation

To induce a measurable signal in MRI, we need to detect and measure the magnetization M. At thermal equilibrium, M is aligned along B_0 which makes it difficult to detect M since the main magnetic field is much larger than the magnetization. Thus, a radiofrequency (RF) magnetic field pulse B_1 is orientated in the x-y plane direction will help to tip the magnetization by a certain angle known as "flip angle" which can be determined by the strength and duration of the RF pulse. B_1 is applied at the Larmor frequency to tip M away from B_0 cause a resonance phenomenon. Once the magnetization is tipped, it will start to precess around the axis of B_0 (figure 2-2) and M can be

easily detected according to Faraday's law of induction that states that this precession will result in a signal called free induction decay (FID).

The total main static field will therefore consist of B_0 the B_1, B= B_{0+} B_1. Contradictorily to the main magnetic field, B_1 is not a static field. Therefore, a time-variant field $B_1(t)$ is given by:

$$B_1(t) = B_{1x}(t)\hat{x} + B_{1y}(t)\hat{y} \tag{2.7}$$

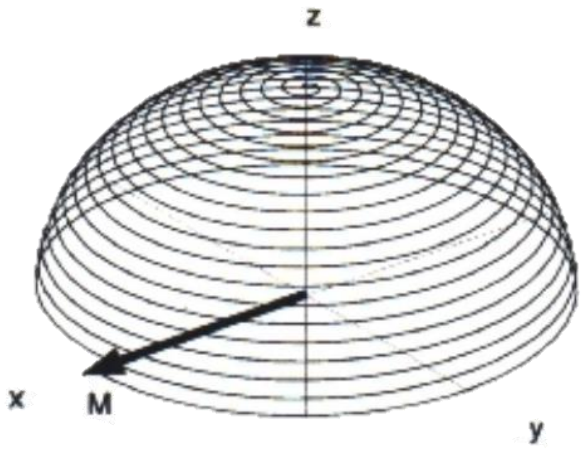

Figure 2-2: The Rf pulse excites and tips the magnetization causing to precess towards the x-y plane. Figure reproduced from Principles of Magnetic Resonance Imaging (2010) by D. Nishimura.

2.3 Relaxation mechanism

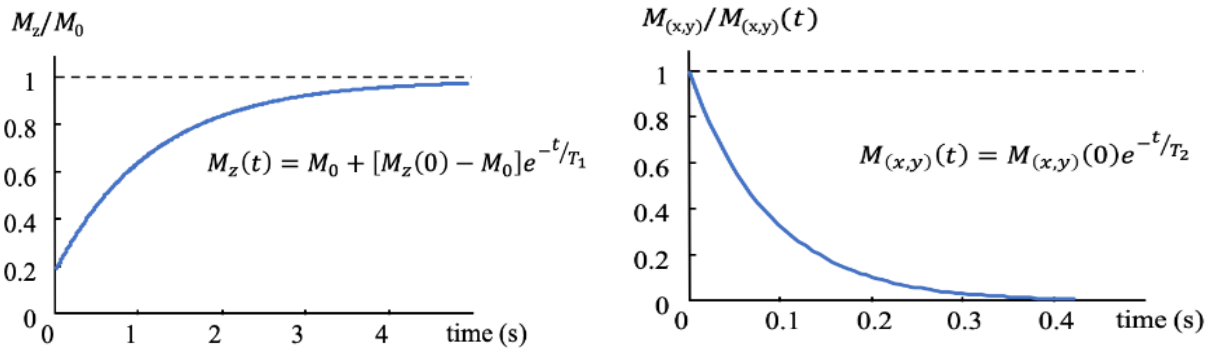

Figure 2-3: Recovery of the longitudinal magnetization through T_1 relaxation and decay of the transverse magnetization through T_2 relaxation. Image modified from [57]

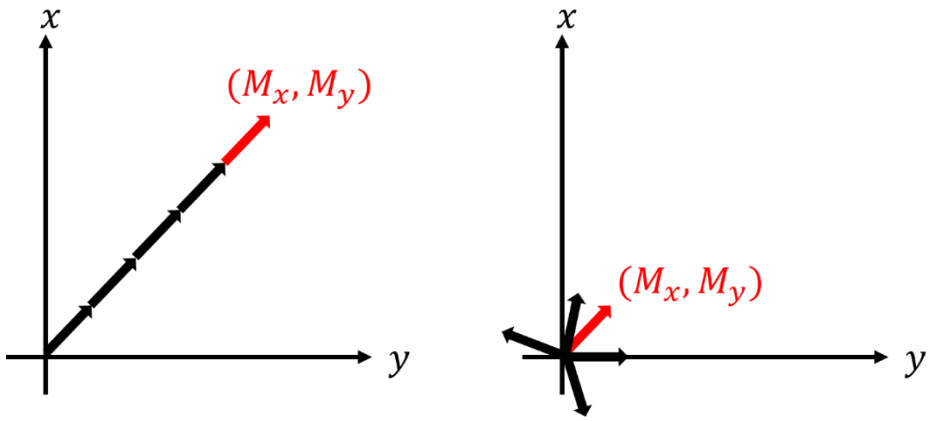

Figure 2-4: Spins dephasing of the transverse magnetization represented as vectors.

Following the excitation, the RF pulse is turned off. If the magnetization is in a non-equilibrium state, it tends to realign itself with B_0 by accumulating all the spins to an equilibrium distribution. This phenomenon is called relaxation. Relaxation can be described by two main concepts longitudinal relaxation (T_1) and transversal relaxation (T_2). These two mechanisms can be modeled using the following equations:

Longitudinal relaxation: $\frac{dM_z}{dt} = -\frac{M_z - M_0}{T_1}$

Transverse relaxation: $\frac{dM_{xy}}{dt} = -\frac{M_{xy}}{T_2}$

Where T_1 can be defined as longitudinal or spin-lattice relaxation time, the T_1 value can be easily identified in figure 2-3 as the time taken for the longitudinal magnetization to reach 63% of its equilibrium value. T_2 is the transverse or spin-spin relaxation time that is also deduced from figure 2-3 as the time taken for the transverse magnetization to decay 63% of its equilibrium value.

On the first hand, the spins have a strong coherence between them, but the molecular tumbling, combination of rotation, vibration, and diffusion cause random effects causing dephasing of the spin or more simply, the spins are spear out in different directions. The spin dephasing effect is illustrated in figure 2-4 which shows that after excitation, the spin will dephase as a function of time. This effect thus results in a decrease in the transverse magnetization. Therefore, the transverse

magnetization will decay in an exponential process. These will lead us to define an additional transverse decay time T_2':

$$\frac{1}{T_2^*} = \frac{1}{T_2} + \frac{1}{T_2'} \tag{2.8}$$

On the second hand, the longitudinal magnetization will recover to its original state until equilibrium. Combining all these different concepts, the dynamics of magnetization is described by Bloch equation:

$$\frac{dM}{dt} = M \times \gamma B - \left(\frac{M_x}{T_2}\right)\hat{x} - \left(\frac{M_y}{T_2}\right)\hat{y} + \left(\frac{M_0 - M_z}{T_1}\right)\hat{z} \tag{2.9}$$

Assuming that the magnetization at equilibrium is $M(0) = [M_0, 0, 0]$ and the presence of the main static field only the solution of the Bloch is:

$$M_x(t) = M_0 \cos(\omega_0 t) e^{-t/T_2}$$

$$M_y(t) = -M_0 \sin(\omega_0 t) e^{-t/T_2} \tag{2.10}$$

$$M_z(t) = M_0 \left(1 - e^{-\frac{t}{T_1}}\right)$$

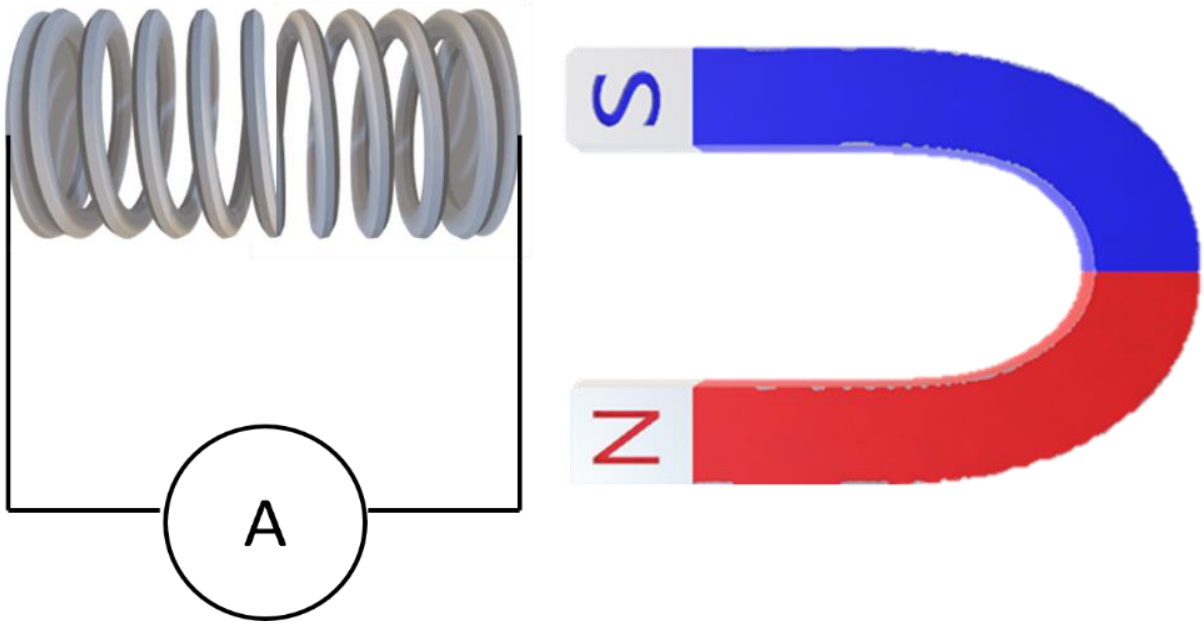

Figure 2-5: Faraday's law experiment that presents a conducting loop (coil) with a main magnetic field symbolized as magnet alongside an ammeter to measure the electric current.

2.4 Complex signal detection

Magnetic induction, one of the fundamental principles of electricity and magnetism, is how receiver coils function. Faraday's Law asserts that a change in magnetic flux via a closed loop, also called a coil, will produce an electric field along the coil, Maxwell-Faraday equation describes this phenomenon:

$$\nabla \times E = -\frac{\partial B}{\partial t} \tag{2.11}$$

Where, ∇ is the curl operator, E is the electric field and B is the magnetic field.

As mentioned before, after the magnetization is tipped, it will undergo precession and relaxation. The magnetic field of M will follow along, resulting in a time-varying magnetic field in the transverse plane. This is why the coil should be placed along the x-y plane. Therefore, the signal is proportional to the transverse magnetization over the volume:

$$signal \propto \int_{volume} M_{xy}(t)\, dr \tag{2.12}$$

Figure 2-5 illustrates Faraday's law. Although modern coils are more complicated in this figure, a loop wire is sufficient to explain the phenomenon. A current that can be precisely and accurately measured will appear to be the electric field along the coil. We can calculate the frequency of the precession, from the size and direction of the current generated through this coil. In order to record this signal that we must have two coils oriented orthogonally.

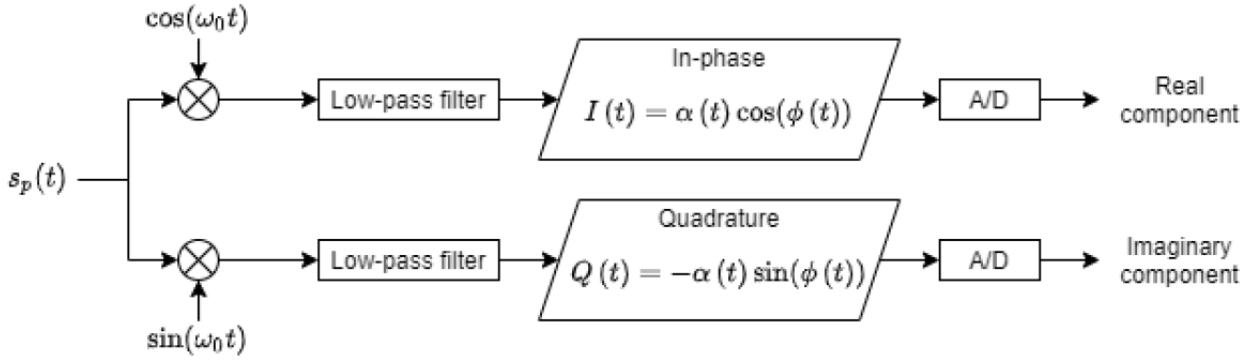

Figure 2-6: Representation of signal detection with the in-phase and quadrature coils after using a low-pass filter to obtain the real and imaginary components of the signal. Image adapted from [10]

The signal recorded oscillates at the Larmor frequency, which can be removed through low-pass filters and demodulation of the signal (multiplying the signal by sinusoidal function) which gives us two outputs corresponding to the real and imaginary components of the signal presented in Figure 2-6. Therefore, a magnitude and phase signal can be calculated using trigonometry and presented in Figure 2-7:

$$Mag = \sqrt{Re^2 + Im^2}$$

$$\emptyset = tan^{-1}\left(\frac{Im}{Re}\right)$$

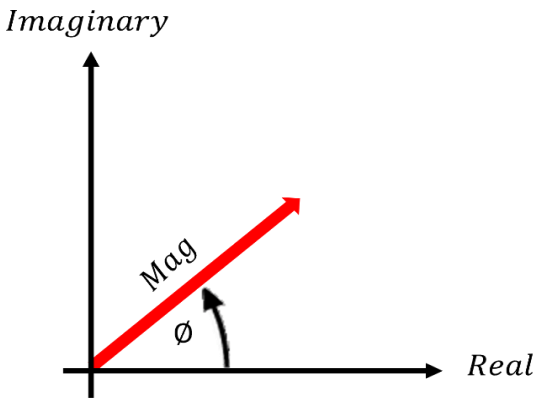

Figure 2-7: Representation of the MR signal in terms of real and imaginary components

2.5 Magnetic field gradients

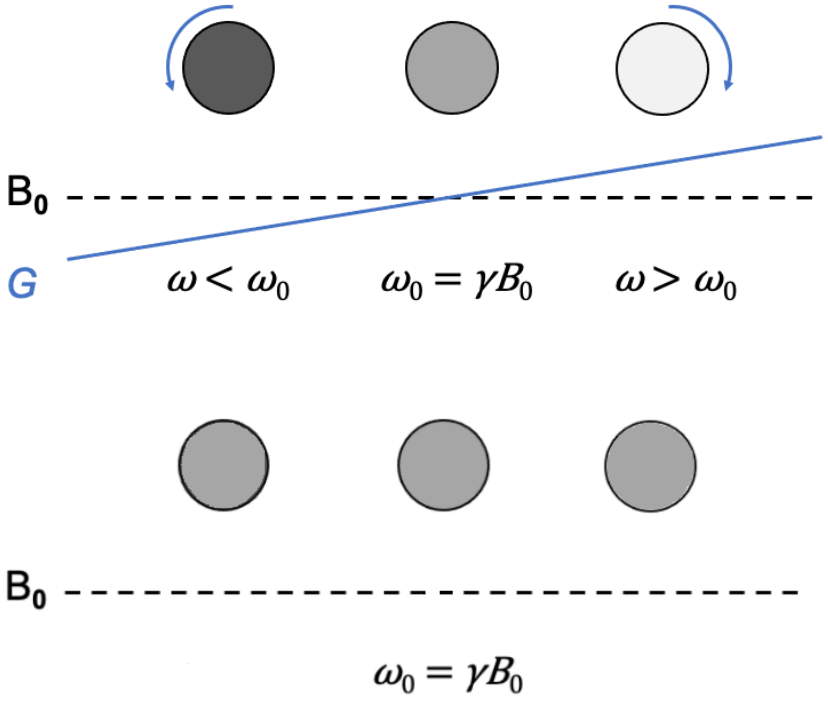

Figure 2-8: Example on different in contrast with magnetic field gradient and without Image modified from [57]

Introducing a magnetic field gradient is a major step in MRI imaging by adding a linear field gradient, relatively small compared to the main magnetic field, in addition to the B0 field to the z-component of the static magnetic field. This results in a spatial dependence in the resonance frequency of all present species. Any orientation may influence the gradient. The magnetic field's z-component varies as a function of the gradient field depending on where you are in the field. The field gradient is also designed such that the variation is zero at the center point and increases (or decreases) linearly with the distance from this point. The gradients can be applied in three orthogonal directions x, y, and z:

$$G_x = \frac{dB_z}{dx}, G_y = \frac{dB_z}{dy}, G_z = \frac{dB_z}{dz} \tag{2.13}$$

The field gradients introduce variations in the z-component of the local field $\vec{B} = B\hat{z}$. The variation can be introduced along any arbitrary direction by combining the 3 gradient axes, but it always modifies the amplitude of the z component of the static B field:

$$\vec{B} = \left(B_0 + G_x x + G_y y + G_z z\right)\hat{z} = B_z(r)\hat{z} \tag{2.14}$$

In Figure 2-8, without the gradient field, the entire signal is at the Larmor frequency of the substance. The gradient field introduces a linear frequency variation in space, and the signal becomes more complicated, while with a magnetic field gradient we can see the difference in contrast between the elements that a part of the signal will be below the Larmor frequency and the other part will be higher than Larmor frequency.

2.6 Gradient echo sequence and k-space sampling

To complete image reconstruction, an appropriate pulse sequence for spatial encoding must be designed. An MR pulse sequence is considered the combination of RF pulses and gradients, which, through different direction, parameters, and timing, manipulate the magnetization into a detectable precessing state. In MRI, Fourier space (k-space) is a multidimensional space which the Fourier transform maps into a function. K-space is typically represented by two spatial frequency coordinates, kx which represents the readout direction of the image, and ky represents the phase encoding direction. The gradient pulses enable us to travel in the Fourier space of the image to collect data in the ky direction. Once we acquired enough k-space information, we can reconstruct the image by a simple inverse 2D Fourier transform.

The most two famous MR sequences in imaging are spin-echo and gradient-echo. Nevertheless, only gradient echo will be discussed here and explored in detail since this imaging sequence will be relevance to next chapters.

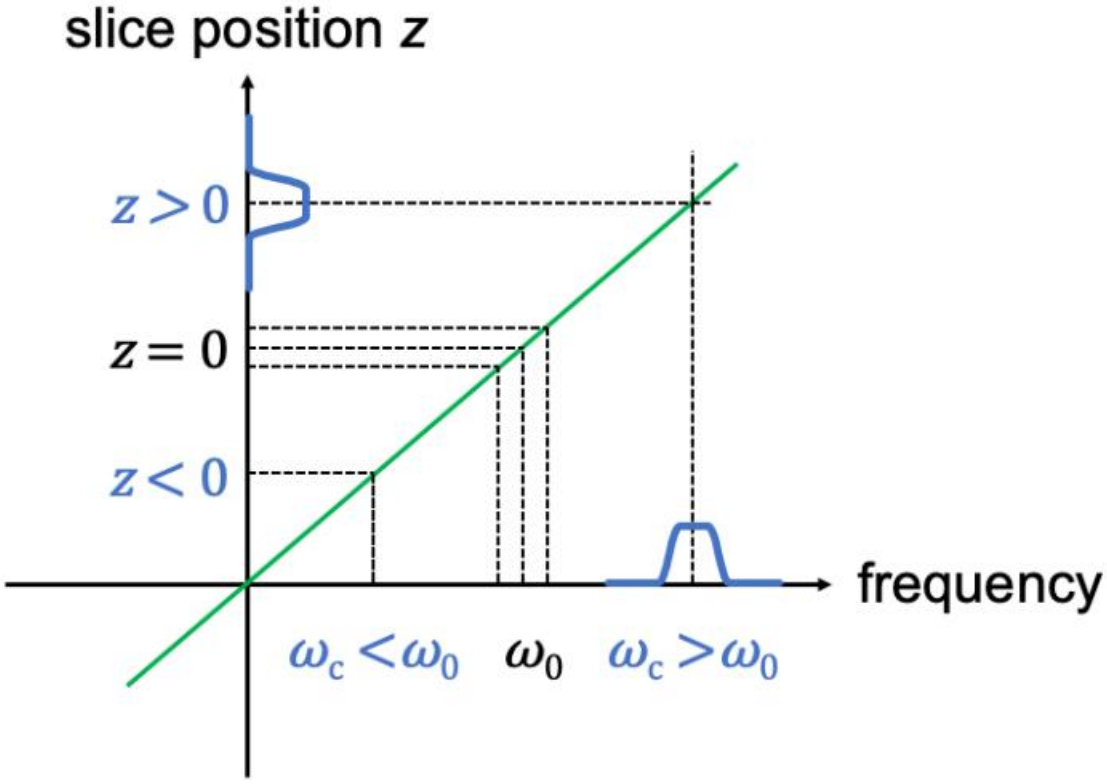

Figure 2-9: Slice selection illustration. Image modified from [57]

In 2D gradient-echo sequence, a slice from the region of interest is selected by exciting only the nuclei in that region by using a RF pulse in the frequency band corresponding to the frequency of the spin is the desired slice. The slice thickness depends on the combination of two things: the gradient amplitude and the RF pulse bandwidth. The on-resonance spins are at the center frequency of the pulse, and therefore, the excited slice will be at the location of the spins that precess at the RF pulse frequency, as demonstrated in Figure 2-9. Once the slice is selected, the phase-encoding gradient is used to encode the information in the phase signal. More precisely, the phase-encoding gradient selects a line in k-space to be acquired. In addition, the readout gradient, also known as frequency encoding, is used to encode the spatial information in the frequency of the signal. In other words, the frequency-encoding gradient transversing the selected line in the phase encoding step while the signal is being collected.

One of the main differences between the 2D and 3D imaging is that, unlike 2D, 3D sequences don't have a slice selection like 2D, but the whole volume is excited, which will impressively improve the SNR. But the disadvantage of 3D imaging is the additional scan time since we have an addition phase encoding direction.

The parameters that affect the contrast in GRE sequences are the flip angle, TR, and TE. The effect of TR, TE and the flip angel is summarized in the Table 2-1. The amount of residual transverse magnetization present prior to the RF excitation varies depending on how these parameters are combined. This residual magnetization manifests when TE and TR are insufficient for a certain flip angle, leaving insufficient time for full T_1 relaxation. Although the quantity of transverse magnetization that remains before the RF pulse varies from cycle to cycle, after the first few cycles, this value stabilizes to a steady state. However, additional considerations are needed when deciding whether to remove this residual transverse magnetization. Transverse magnetization can be eliminated by utilizing RF spoiling and variable gradient spoiling.

Table 2-1: Contrast in a GRE sequence as functionof flip angle, TE, and TR. The information presentaed in the table was collected fom R. Hashemi, W. Bradley, and C. Lisanti, "MRI : the basics." Wolters Kluwer Health,

Contrasts

Parameters	Proton Density Weighted	T1 Weighted	T2 Weighted
Flip angle	Small ($5^0 to\ 30^0$)	Large ($60^0 to\ 90^0$)	Small ($5^0 to\ 30^0$)
TE	Short (2-5 ms)	Short (2-5 ms)	Long (10-100 ms)
TR	Short/Long	Long ($\sim 100\ ms$)	Short (TR$< 3T_2^*$)

Different methods can be applied to speed up the spatial encoding of the spatial frequency information in k-space. Partial Fourier, or the collection of only a portion of the data in k-space, is the first method for reducing the scan time. By extrapolating the missing information from the mathematical principles, the symmetry of k-space enables the reconstruction of an image with little

over half of the lines in k-space. Parallel imaging is another strategy to shorten the scan time. The concept behind parallel imaging is to collect imperfect k-space data, which would typically cause aliasing, and to fill in the gaps by using the spatial sensitivity data from several receiver coil components. Sensitivity encoding (SENSE) is one instance of a parallel imaging approach that is widely being used.

2.7 Quantitative susceptibility mapping

Quantitative MRI refers to the use of MRI techniques to extract data that can represent the physical, physiological, functional, or microstructural characteristics of the tissue. The collected data can provide important information for diagnosis and treatment in various medical applications. Quantitative MRI has highly repeatable and reproducible as shown in recent studies [12]. Quantitative susceptibility mapping (QSM) is an emerging quantitative MRI technique that computes the magnetic susceptibility distribution of the underlying tissue using the phase component of MRI data to extract the magnetic susceptibility [13]. QSM uses susceptibility as its contrast method. Phase data acquired in MRI needs to be carefully processed before they can be used for QSM because the accuracy of susceptibility maps is directly dependent on the quality of the phase processing.

QSM can be used in a wide variety of fields, especially for brain analysis, making it one of the most interesting techniques for MRI. QSM highlights aspects of anatomy that have prominent susceptibility values, such as blood. Thus, one useful aspect of QSM is to identify micro bleeds in traumatic brain injury studies [1]. Another main aspect of QSM is to quantify the brain oxygenation, which can be useful to identify the health state of the brain. Magnetic susceptibility is a fundamental physical quantity that is a measure of how much a material will be magnetized in an applied external magnetic field. Thus, we can identify two categories of material: on the first hand, paramagnetic materials respond to the external magnetic field by aligning with this field (parallel), thus adding to the external field, therefore, paramagnetic materials have positive susceptibility. On the second hand, diamagnetic materials that align against the magnetic field (anti-parallel), thus subtracting from the magnetic field, therefore, diamagnetic materials have a negative susceptibility. The behavior of paramagnetic and diamagnetic materials is illustrated in Figure 2-10. Consequently, we can identify this equation:

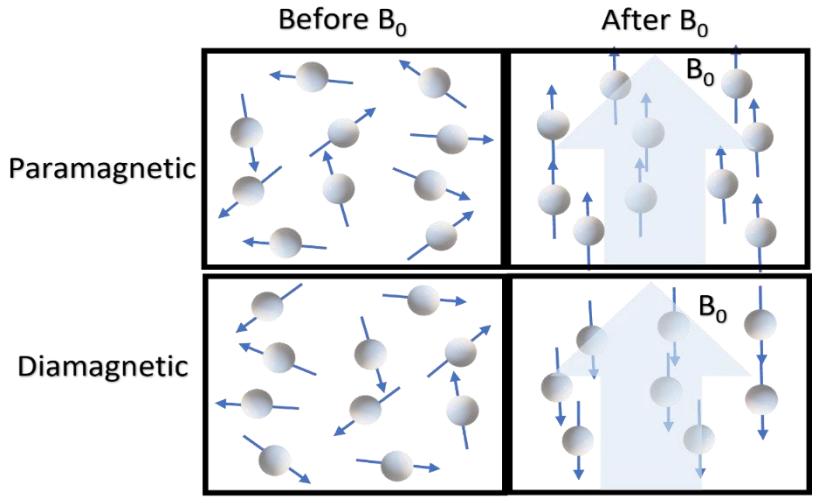

Figure 2-10: Schematic representation of paramagnetic and diamagnetic material before and after applying a magnetic field.

$$M = \chi_M B \tag{2.15}$$

where B is the applied magnetic field, χ_M is the magnetic susceptibility, and M is the resulting magnetization.

Table 2-2 lists some tissues of the human brain and their known susceptibility values.

Table 2-2: Susceptibility values of common anatomical structures of the human brain, the table is separated into diamagentic and paramegtic . The susceptibility values are expressed relatve to CSF this is why its value is zero. Table assembled from W. Li et al., "Q uantitative susceptibility mapping of human brain reflects spatial variation in tissue composition," Neuroimage, vol. 55, no. 4, pp. 1645–1656, 2011, doi: 10.1016/j.neuroimage.2010.11.088

Brain structure	**Susceptibility χ**	**Brain structure**	**Susceptibility χ**
Paramagnetic:		**Diamagnetic:**	
CSF	$0 + 0.019$	**Genu of corpus collosum**	-0.033 ± 0.013
Red nucleus	0.087 ± 0.028	**Splenium of corpus collosum**	-0.038 ± 0.013
Globus pallidus	0.043 ± 0.02	**Sagittal stratum**	-0.075 ± 0.019
Caudate nucleus	0.019 ± 0.012	**Capsula interna**	-0.002 ± 0.012

The contrast in susceptibility maps is caused by the susceptibility variation between tissues. The strongest susceptibilities are found in the structures that produce the greatest contrast. Therefore, depending on the tissue, the source of contrast varies. Lipids are the primary source of contrast in WM as a result of axon myelination. Iron-rich compounds that are extremely paramagnetic are what cause the contrast in deep brain tissue like the putamen, globus pallidus, thalamus, and caudate nuclei [14]. Although QSM has found many applications for imaging the brain, its use in other regions of the body is an active field of research. But this work will focus on brain QSM application.

The 3D mGRE pulse sequence is the one that is most frequently utilized to produce MR complex data for QSM. The GRE can be substituted with other acquisition strategies. The research for QSM also uses other data acquisition methods, such as balanced Steady-State Free Precession (bSSFP) [15], Magnetization-Prepared Two Rapid Acquisition Gradient Echoes (MP2RAGE) [16], and multi-flip angle data collected using Strategically Acquired Gradient Echo (STAGE) [17]. However, this work is solely based on 3D mGRE data acquisition.

QSM measurements are relative because the susceptibility values of a given material depend on the local magnetic field and the properties of the surrounding tissue. Therefore, susceptibility values are not absolute values. Therefore, it is important to ensure that the samples being compared were measured under the same conditions and with the same equipment in order to obtain meaningful comparisons. In QSM, phase information is combined with several post-processing techniques to estimate the susceptibility distribution. QSM imaging can be divided into two categories: single orientation imaging and multiple orientation imaging, also known as COSMOS. The main steps for the phase processing for single orientation are phase unwrapping, background field removal, and dipole inversion. In the literature, different techniques have been proposed for each step. COSMOS shares most of the procession steps with the single orientation acquisition, and details will be given later in this chapter. The main objective of this work is to explore and test different QSM reconstruction algorithms and techniques and compare them specifically for a neonatal population because of the lack of QSM studies done for this population.

The following section will present a detailed explanation of each QSM phase processing step. In addition, it will present a review of the literature for the different techniques used to reconstruct a QSM image.

2.8 Background on QSM pipeline

2.8.1 Masking

Masking is a major step should be applied before the reconstruction QSM image to identify the region of interest (ROI). The mask should ideally eliminate any possibly problematic areas where the dipole inversion step would have trouble correctly interpreting the susceptibility. These problems can occur in regions with quickly changing phases (at the tissue/air interfaces). There are a few approaches to getting a mask, but the majority of them use the MRI scan's magnitude data to extract the region of interest. The FMRIB Software Library, developed by a team at Oxford University, is a well-defined tool for brain QSM, which is the subject of this work [18]. There is a brain extraction tool (BET) that offers a precise mask of the brain in this software library [19]. Only a magnitude image, acquired synchronously with phase data, is needed by the FSL BET tool. The BET is an iterative function that starts by creating an intensity histogram in order to determine the image's bottom and upper-intensity values.

2.8.2 Phase unwrapping

The next step of this pipeline is phase unwrapping. Phase unwrapping is an important problem in signal-processing problems. The values of the wrapped phase images are encoded in the range of ($-\pi$ to $+\pi$). However, the values of the true phase can be extended up to 2π. Any value that is outside this range of ($-\pi$ to $+\pi$) will be returned to it, causing discontinuities in the phase and inaccuracy in the results [20]. Therefore, phase unwrapping consists of removing these discontinuities in phase images caused by the limited mathematical interval of the reconstructed phase values.

The literature suggests a wide range of methods for unwrapping phase data. The trade-off between computing time and algorithm accuracy frequently determines which one to use [1]. A visual representation of how a phase unwrapping algorithm can remove all discontinuities as presented in

Figure 2-11, which is a comparison between a brain phase image from an MRI scanner and the same image after phase unwrapping.

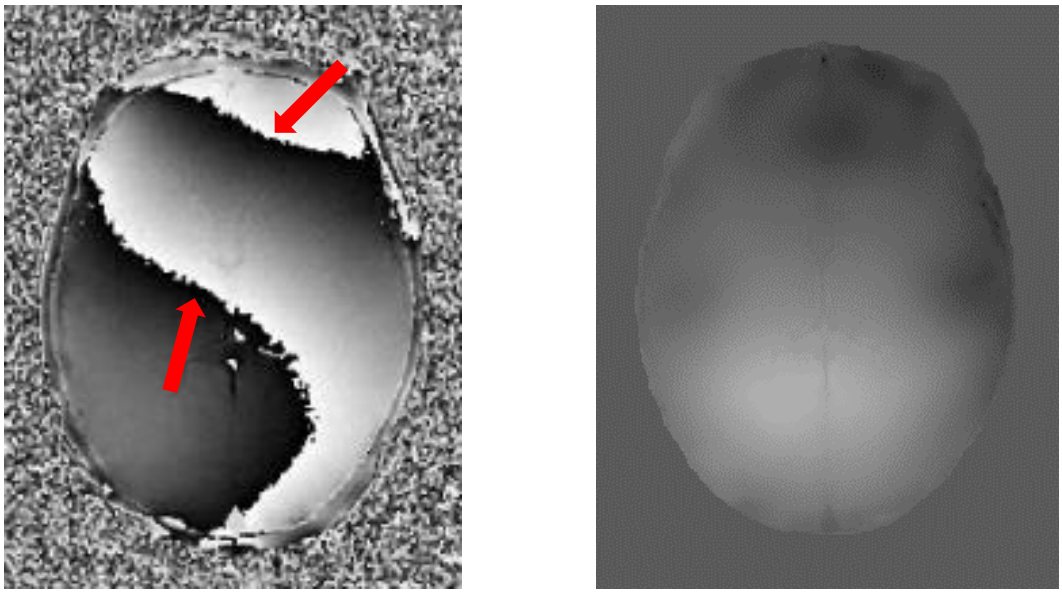

Figure 2-11: Measured wrapped phase in the brain with red arrows indicating the phase wrap, and the unwrapped phase for the same brain.

In general, phase unwrapping algorithms can be classified into two categories: spatial and temporal techniques. On the first hand, spatial unwrapping is the process of reducing gaps between neighboring pixels, either inside each slice for 2D unwrapping or in a 3D volume for 3D unwrapping. It can be applied to single-echo or multi-echo data. This includes path-based strategies such as quality-guided procedures [21] and region-growing strategies [22], as well as Laplacian-based strategies, either continuous [23] or discrete [1]. Three methods of spatial unwrapping will be described in this work. In the second-hand, temporal phase unwrapping techniques consist of removing discontinuities between successive echoes and thus, it requires data from at least two TE. Temporal phase unwrapping is usually performed by calculating the phase difference between two successive echoes and adding multiples of 2π when the difference exceeds π [24]. Only when the phase accumulation between the two succeeding echoes has a single-phase wrap is proper temporal unwrapping with equally spaced echoes achievable. This needs very narrow echo spacing that is frequently not usually accessible [25]. The use of irregular echo spacing can solve this issue. The unwrapping multi-echo phase images with irregular echo spacings (UMPIRE) procedure, which

needs three irregularly spaced echoes, is an illustration of a temporal unwrapping algorithm [26]. Let's first start with spatial phase unwrapping techniques:

On the first side for spatial methods, Continuous Laplacian (CL) phase unwrapping consists in calculating the unwrapped phase using the Laplacian (∇^2) of the wrapped phase ($\emptyset_w$) as mentioned in the following equation [23]:

$$\nabla^2 \emptyset_{uw} = \cos(\emptyset_w)\, \nabla^2(\sin(\emptyset_w)) - \sin(\emptyset_w) \nabla^2(\cos(\emptyset_w)) \tag{2.16}$$

This equation allows the calculation of the Laplacian of the unwrapped phase. Using the presumption of image continuity [23], the unwrapped phase can then be recovered using the inverse Laplacian operator [1]. This method is based on two presumptions: that the field of view is infinitely large and that the phase is a continuous function.

Second, Discrete Laplacian (DL) phase unwrapping consists of calculating the finite difference between the wrapped phase of the central pixel $\emptyset_{w,c}$ and its neighbors $\emptyset_{w,i}$:

$$\nabla^2 \emptyset_{uw} = \sum_{i=1}^{n} \arg\,[e^{i(\emptyset_{w,i} - \emptyset_{w,c})}] \tag{2.17}$$

This is the result of the convolution between the discrete Laplacian kernel with the unwrapped phase. Thus, the unwrapped phase can be recovered using deconvolution of the convolution result [1]. With this method, the presumptions of continuous functions and an unlimited field of vision are avoided. As MRI data are discrete and have a small field of view, this is therefore more representative of MRI data.

Third, region-growing (RG) phase unwrapping, when the difference between two neighboring voxels is greater than π, this unwrapping algorithm involves adding the necessary multiple of 2π. Starting with a seed placed in a region with a smooth phase, the unwrapped region is gradually expanded by observing the phase difference between neighbors. Multi-seed unwrapping refers to

the process of using multiple start points and merging the end areas to finish the unwrapping. Region growing does not alter the initial phase values if there is no phase wrap, in contrast to Laplacian-based unwrapping [22].

Finally, quality guided (QG) phase unwrapping. The quality guided strategy is similar to region-growing unwrapping, but involves unwrapping the highest-quality voxels first and using a quality map to direct the unwrapping process. For quality guided unwrapping, several of the quality maps can be defined and used [27]. The data is often unwrapped using a region growing strategy, but quality guided unwrapping approaches are far more resilient than normal region-growing algorithms since low quality voxels, such as highly wrapped or noisy regions, are unwrapped last, preventing the propagation of errors during the unwrapping process [28].
Due to the assumption of spatial continuity and smoothness in phase images that spatial unwrapping methods rely on [29], they typically do not produce reliable findings when there are steep phase gradients in images [25]. When used with multi-echo data, spatial unwrapping involves individually unwrapping each echo image, which can lead to mistakes in the presence of excessive noise and discontinuous regions. Quality guided techniques have shown tremendous promise in overcoming these problems [27]. As a result, when the phase evolution in a voxel between two successive echo times (TE) is greater than 2π (from $-\pi\ to + \pi$), 2π jumps between successive echo volumes may happen. In certain circumstances, both spatial and temporal unwrapping are necessary.

On the other side for temporal methods, the UMPIRE algorithm is constrained due to its sensitivity to noise and the fact that commercial MRI scanners do not always have access to sequences with unevenly spaced echoes, Additionally, spatial unwrapping is frequently necessary in addition to temporal unwrapping because the former is unable to resolve 2π phase offsets between adjacent voxels.

Overall, phase unwrapping remains an open question in the presence of steep phase gradients and for multi-echo data. Implementations of Laplacian-based unwrapping is still one of the most

famous used phase unwrapping techniques due to its availability, simplicity, robustness, and fast calculation [23].

2.8.3 Background removal

After obtaining the unwrapped phase for each echo and combining all echoes into a single map containing information about the magnetic field shift, the next key step in the QSM pipeline is background field removal. There is an unwanted background field that taints the field map of the brain that is directly calculated from recorded phase images. While we are primarily interested in the local field map that derives from magnetic susceptibility sources within the voxel, the background field is caused by systemic B0 field nonuniformity and macroscopic magnetic susceptibility variations outside the brain tissues of interest, such as air and bone, these contributions are defined as background magnetic fields, and they need to be removed to determine the local field [30]. In other words, background removal consists in isolating the local field (B_{int}) generated by dipoles located within tissue voxels in a defined region of interest (ROI) that are desirable for the QSM process, from the background field (B_{bkg}) generated by dipoles outside of this predefined ROI:

$$B_{total}(\vec{r}) = B_{int}(\vec{r}) + B_{bkg}(\vec{r}) \tag{2.18}$$

Therefore, a robust background field removal algorithm is important to dissociate meaningful information with background information to achieve optimum QSM images. High pass filtering was a widely used background field removal techniques before the invention of QSM. This eliminates the data's low spatial frequency component. With this method, the background field is virtually eliminated. Homodyne filtering is a typical high-pass filter type [31]. Because homodyne filtering eliminates all the significant phase changes that cause phase wrapping, it may be applied immediately to wrapped phase images, which speeds up processing. Homodyne filtering is quick and simple to use, but it eliminates all the data's low frequency components, including significant information that does not match the background. As a result, susceptibility levels are drastically underestimated, and susceptibility maps may contain anatomical inaccuracies. Because of this,

background field removal with high pass filtering of the phase is only acceptable when small-scale phase variations are of interest [30]. On the first hand, current background removal techniques assume that the local and background field are separable polynomials [32]. The assumption of separability between local fields and background field in some space is often violated and often not fully available or accurate enough, especially when there are significant variations in sensitivity outside of the imaging field of view leading to inaccurate background field. On the second hand, other methods can estimate the background field. In this method, the sample in the ROI is replaced by uniform materials with a known susceptibility, then the background field is calculated by subsequently calculating the difference between the total field and the known local field. But for clinical data acquisition, however, such a scan is impractical or impossible to perform.

Several enhanced background field removal algorithms were introduced with the creation of QSM. The main three background field removal techniques are: projection onto dipole (PDF) [32], sophisticated harmonic artefact reduction for phase data (SHARP) [13], and Laplacian boundary value (LBV) [33].

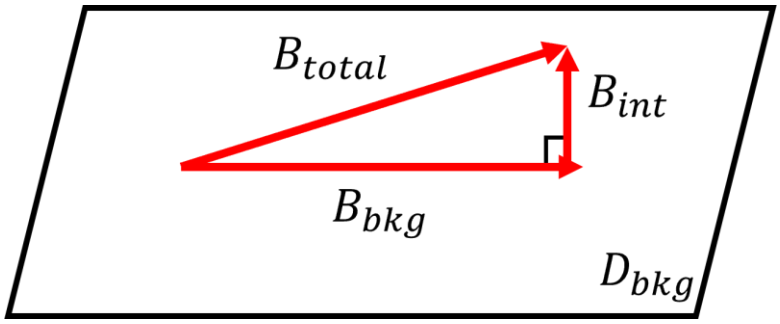

Figure 2-12: Illustration of the relationship between background and local fields

First, projection onto dipole (PDF) is a technique inspired by the projection theorem in Hilbert space, as it projects the total field produced by the region of interest onto the space that is spanned by all background unit dipole fields (D_{bkg}) as illustrated in Figure 2-12. PDF method relies on the approximately orthogonal relationship between the local and the background field. The background susceptibility distribution (χ_{bkg})can be found by solving the minimization problem described in the following equation:

$$\chi^*_{bkg} = argmin_{\chi_{bkg}} \left\| W\,(B_{total} - d \otimes \chi_{bkg} \right\| \tag{2.19}$$

Where W is a weighting matrix generated from the accompanying magnitude images acquired by the same multi-echo GRE sequence [34]. Then, the true local field can be estimated as $B_T^* = B_{total} - d \otimes \chi_{bkg}$, where B_T^* is an element of the space covered by all the background unit dipole fields. This method works well except at the brain boundaries where the orthogonality assumption breaks down.

Second, sophisticated harmonic artefact reduction for phase data (SHARP) technique separates the magnetic fields by imposing the background fields as harmonic fields as opposed to local fields generated by dipoles inside the object, which are not harmonics. By exploiting the mean value property of harmonic functions to solve the differential equation, the local field can be separated from the background field based on this harmonic property:

$$\nabla^2 B_{total} = \nabla^2 B_{int} \tag{2.20}$$

The local field is isolated using the harmonic mean value theorem, which asserts that any harmonic functions are preserved following the convolution with a normalized function.. A modified version of SHARP algorithm, called regularization enabled sophisticated harmonic artefact reduction for phase data (RESHARP) [35], uses regularization in combination with SHARP, which was an improvement from SHARP, thus, reducing the residual background during the elimination of the background field:

$$argmin_{B_{int}} \| M\,(\delta - \rho) \otimes (B_{int} - B_{total} \|_2^2 + \lambda \| B_{total} \|_2^2 \tag{2.21}$$

Where M is a binary mask defining the brain ROI with a value 1 inside the brain and 0 outside, λ is the regularization parameter that balances the data fidelity and residual errors, and is often selected using L-curve analysis and δ is the unit impulse at the center of the radial function ρ. The ROI is eroded by SHARP and RESHARP, which causes erroneous susceptibility at the ROI's edges. When the structures of interest are around the ROI's center, this is typically not a problem.

To solve this problem, another variation of SHARP, called variable kernels sophisticated harmonic artefact reduction for phase data (VSHARP), uses varying radius kernels that decreases in regions close to the ROI boundary [36].

Finally, Laplacian boundary value (LBV) removes the background field by explicitly resolving the Laplacian boundary value problem. The value of the local field at the ROI border is taken to be zero in order to define the boundary conditions, while the value of the background field is taken to be the same as the value of the total field. The background field is typically one or two orders of magnitude larger than the local field, making this approximation possible.

In conclusion, even though a priori assumptions make it possible to distinguish background and internal fields uniquely, the uniqueness of the solution is not a guarantee of the accuracy of the internal field estimation, especially in regions where the assumed physical or mathematical assumptions fail. Research is still being done to find the appropriate solution to the background field removal issue in QSM. The objective is to develop a method that results in precise local field estimation. There is still a need for improvement in the areas of background removal for accurate QSM in the presence of high susceptibility structures and accurate susceptibility estimation at the margins of the ROI.

2.8.4 Dipole inversion

After applying the phase unwrapping and background removal algorithms, the next step is to estimate the local field map by applying a dipole inversion technique, which is the main the step to extract the susceptibility value for each voxel and thus creating a susceptibility map. There are numerous suggested techniques to complete the dipole inversion, much like the preceding steps. Given that the problem is ill-posed, it becomes more and more challenging to assess the accuracy of the solution to the dipole inversion problem. The ill-posed problem can be simply explained by the Fourier transform of the dipole field kernel $\left(D(k)\right)$ according to the following equation:

$$D(k) = \frac{1}{3} - \frac{k_z^2}{k^2} \tag{2.22}$$

Where $k^2 = k_x^2+k_y^2+k_z^2$, $k_x, k_{y,} k_z$ are k-space coordinates. Thus, the inverse Fourier transform to the dipole field it will be equal to zero at a magic angle (54.7°). The major challenge in directly inverting the equation to solve for χ is that when $3k_z^2 = \left|\vec{k}\right|^2$ represented in Figure 2-13, the division by zero problem arises in the imaging domain, resulting in severe streaking artifacts in the reconstructed susceptibility maps [25]. It is theoretically possible to resolve this ill-posed problem by collecting data N times with the subject oriented differently from the main field and filling in the gaps at the zero regions. Calculation of Susceptibility Through Multiple Orientation Sampling (COSMOS) is the name of the computational solution for this multi-orientation scheme. COSMOS is recognized as the golden standard of QSM reconstruction [37]. COSMOS typically employs a minimum of three orientations for sampling and reconstruction. The regions that are problematic in one measurement become behaved in another measurement due to the change of orientation. However, COSMOS is challenging to implement in human beings and necessitates a lengthy data gathering period. As a result, to get around the inversion problem's ill-posed for a single-orientation acquisition, a regularization term that considers prior knowledge of the susceptibility distribution is frequently incorporated. Therefore, many dipole inversion methods have been developed to overcome this obstacle.

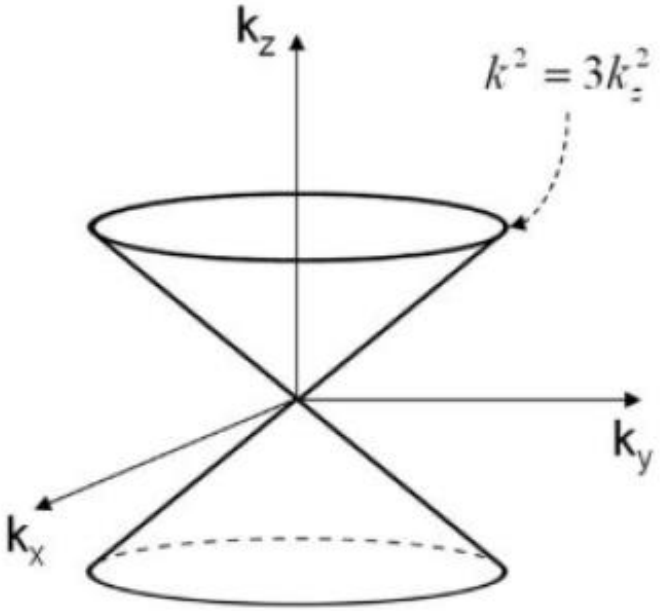

Figure 2-13: Zero cone region in QSM inverse problem. (Figure Adapted from C. Liu, W. Li, K. a Tong, K. W. Yeom, and S. Kuzminski, "Susceptibility-weighted imaging and quantitative susceptibility mapping in the brain.," J. Magn. Reson. imaging, vol. 42, no. 1, pp. 23–41, 2015

The majority of these solutions circumvent this by introducing a threshold to the algorithm, which eliminates values from the k- space where D(k) = 0, and substitutes them with small, non-zero values. Accordingly, artefacts may appear, with the severity varying according to the threshold level, where a higher threshold will move closer to the undesirable D(k) = 0 regions while replacing more useful data. A smaller threshold number preserves more information, however, it may result in artefacts because of transformation errors near D(k)=0.

This idea is the basis of two popular approaches, neither of which calls for a knowledge of the region of interest's anatomical structure beforehand. The Truncated Singular Value Decomposition (TSVD) is one method that illustrates this kind of dipole inversion [38]. Truncated k-space Division (TKD), a TSVD version, is another method that is frequently applied in QSM [31].

Dipole inversion can also be approached using an image technique. In order to derive information about the susceptibility from the phase, these methods essentially minimize functions using the Gauss-Newton method of linear interpolation [39]. First, Tikhonov regularization consists of a data fidelity component in the L2-norm, and tends to smooth the solution within the ROI [40]. Similar to this, the Total variation (TV) regularization term, which is a regularization term in the L1-norm,

is minimized to encourage sparsity [41]. For example, Morphology Enabled Dipole Inversion (MEDI) attempts to sparsify the ROI edge difference by using anatomical priors [42]. Total variation regularization is frequently applied on the basis of the presumption that the local susceptibility distribution comprises piecewise constants that fluctuate smoothly across sparse structural boundaries.

2.9 Neonates imaging and QSM

Neonatal MRI is a specialized form of MRI that is used to visualize and assess the health of newborn babies, typically those who are less than 28 days old. It is a valuable tool for identifying and diagnosing various conditions that can affect neonates, such as brain abnormalities, congenital abnormalities, and neurological disorders.

Neonatal MRI is generally considered safe for newborns, and one of the main differences is that the brain of a neonate is still developing and changing rapidly. This can make it more challenging to obtain high-quality images in this population due to the small size and fragility of neonates, as well as the potential for motion artifacts. Specialized techniques and protocols may be used to ensure the safety and comfort of the infant during the MRI procedure that will be discussed in the following sections.

2.9.1 Environment and training

To set up a good environment for pediatric MRI, it is important to create a child-friendly and comfortable atmosphere in the MRI room. This can be achieved by using bright colors, toys, and other interactive elements to distract and engage the child during the scan [43]. Additionally, it is important to have a trained and experienced pediatric radiologist and technologist to perform the scan and ensure the child's safety and comfort. One way to prepare children for an MRI scan is to provide mock MRI training. This can be done by using a replica of an MRI scanner that simulates

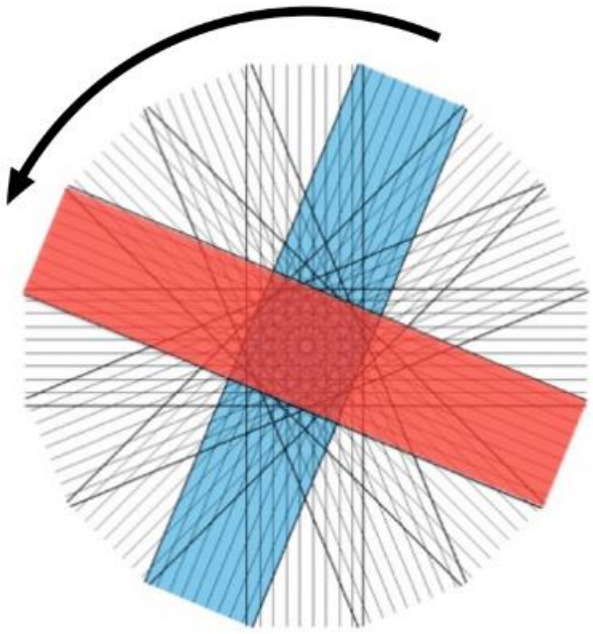

Figure 2-14: PROPELLER sequence sampling blades of data in rotation around the center of k-space. Figure inspired from [59].

the noise and sensation of the actual scan, allowing the baby to become familiar with the experience before the actual scan takes place [44].

2.9.2 Challenges and solutions

First, one of the biggest challenges in neonates scanning is motion artifact. Motion artifacts refer to distortions or blurring in medical images caused by the movement of the newborn during the imaging process. This artifact can be classified into two types: 1) random movements, which is very common among neonates that can't control their movements, 2) periodic motion, such as respiration or cardiac motion. Fortunately, many techniques have been developed to tackle this challenge [45]. One of the easiest solutions to prevent arbitrary motion is using some special equipment to keep the newborn in place, or put the baby to sleep before the scan, or the use of anesthesia and try to finish the scanning as soon as possible. On the first hand, in order to robustly remove motion artifact caused by random movements, several strategies can be done, such as: self-navigated trajectories, prospective correction, and retrospective correction. One of the most common self-navigated trajectories techniques is Periodically Rotated Overlapping ParallEL Lines with Enhanced Reconstruction (PROPELLER) which consists of using radially directed strips,

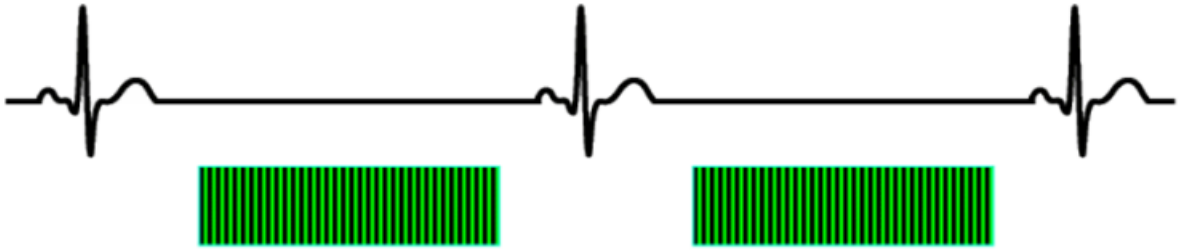

Figure 2-15: Triggering data acquisition during a specific time window to remove periodic motion. Figure inspired from [60].

known as blades, that rotates at a small angle to over-sample the center of k-space (contributes most to image contrast and contains the highest signal amplitude) as shown in Figure 2-14. Although, the reconstruction process will take longer time, this strategy will strongly reduce the artifact results in a higher SNR [46]. Retrospective correction techniques correct acquired data afterwards (post-processing) by considering the translation and rotation in the k-space, but these methods can be computationally expensive. Finally, prospective correction techniques adapt scan to the patient's motion by using external tracking devices or MR navigators to dynamically update the gradients, RF pulses, etc. This technique can work either in image space or k-space domain. Although it showed great results, it needs to be done in real-time and is very dependent on the precision of the tracking data. On the other hand, periodic motion artifacts can be removed using triggering where MR data is acquired only a specific physiological event. Triggering allows for obtaining static images at a specific point in the cardiac cycle which allows us to overcome motion results from cardiac and respiration motion as shown in Figure 2-15 [47].

Second, smaller structures, newborn are in the first stages of development, so all equipment dedicated for adults would not be appropriate to use for neonates. Thus, the importance to develop dedicated pediatric equipment such as RF coils which has gained interest in recent year due to high demand. Smaller coils are much effective (in neonatal imaging) since it maximizes the local signal [48].

Third, MR sequences optimization for neonates. Imaging techniques have been developed specifically for the brain and body of newborn to achieve high-quality images without causing undue disturbance to the newborn. These techniques differ from those used in adults, as the neonatal brain has higher water content, which requires different parameters for T1 and T2 weighting [44]. High-resolution imaging is critical for the small structures of the neonatal brain

and 3-D isotropic volumetric sequences are preferred for better contrast and differentiation between grey and white matter. Efforts are also being made to optimize 3-D sequences for the pediatric population, but this poses some challenges such as respiratory and cardiac motion artifacts since there are long sequences [49]. Conventional MRI may not be able to detect certain neonatal specific condition and high-risk newborns, such as HIE which is particularly challenging to assess with conventional techniques [50]. QSM is becoming more and more popular tool for investigating various diseases and researchers are working to optimize it and make it more suitable for neonates.

2.9.3 Neonatal QSM

QSM can be used to evaluate the brain in neonates with traumatic brain injury, stroke, and other forms of acquired brain injury. The interpretation of QSM images may also be different for babies compared to adults. For example, the iron deposition in the brain of a baby can indicate different things compared to an adult, as iron deposition in the developing brain can be a normal process, whereas in adult brain, it can be an indication of a pathological process. Another difference is that the parameters used in QSM reconstruction may need to be adjusted for babies. For example, the regularization strength and the number of iterations used in the reconstruction process may need to be adjusted to account for the unique characteristics of the developing brain.

QSM techniques have been well developed for adults, but it's not necessarily adapted for the neonatal population because of the anatomical difference between adults and neonates, hence, the importance of investigation these techniques in a pediatric population.

CHAPTER 3 METHODOLOGY

The literature review emphasized the need to compare different QSM reconstruction algorithm to choose the most efficient one. Choosing the correct algorithm can efficiently provide information on patients physical conditions and help clinicians make informed decisions. However, current methods have not been specifically designed with the smaller anatomy of neonates in mind.

Numerous QSM reconstruction techniques have been developed and although their promising results, they have limitations that are currently being studied and may prevent them from being widely used in clinical settings. In addition, the accuracy of these methods and the resulting QSM image quality have not been quantitatively assessed in a clinical setting, in neonates. Several studies have demonstrated the potential of QSM for quantitatively measuring blood oxygenation, and it holds great promise to identify a biomarker of brain injury for neonatal asphyxia that can help to quantify the oxygenation levels.

Therefore, the objective of this thesis is to compare QSM reconstruction techniques on a neonatal population to study the feasibility and efficiency of these methods in a neonatal population. To our knowledge, this is the first research study that compares a large variety of reconstruction methods on neonates. This comparison is challenging since golden standard images (COSMOS) were not available due to the difficulties in obtaining COSMOS neonatal data.

After 72 hours of hypothermia neonates follows this protocol to acquire MRI data: neonates are given anesthesia to keep them still and asleep during the imaging process. This is important to ensure that the images are clear and accurate. Then, the neonates are swaddled in blankets with straps to furthermore secure the babies in the MRI. Once the patient is in the MRI, the machine is programmed with a specific imaging protocol, in our case multi echo gradient echo. The images produced by these sequences will be analyzed by a specialist to assess the extent of brain damage caused by HIE and to plan appropriate treatment for the neonates. For further analysis the magnitude and phase images are used to reconstruct QSM images. Each magnitude and phase echo will then be combined to a single magnitude and phase image before applying a Laplacian phase unwrapping algorithm to the phase image, then, QSM images were reconstruction using 13 different methods by combining the two most important steps for QSM reconstruction: background field removal and dipole inversion, the reconstruction methods were classed into two group:1)

Table 3-1: Summary of selected QSM background removal and dipole inversion algorithms.

Algorithms name	Description
Background field Removal:	
PDF	Projects the overall field onto a lower-dimensional space that is spanned by the background fields.
LBV	Removes the background field by resolving the Laplacian boundary value problem.
ISMV	Relies on the spherical mean value (SMV) of harmonic function using iterations.
SHARP	Separates the magnetic fields by imposing the background fields as harmonic fields.
VSHARP	Utilizes variable sphere kernels size to implement the SHARP property.
RESHARP	Uses Tikhonov regularization to promote a harmonic internal field with small norm.
Dipole inversion:	
MEDI	Inverts the dipole convolution with regularization with anatomic image.
NDI	Estimates dipole coefficients by solving a nonlinear optimization problem.
SSTGV	Incorporates phase unwrapping, background field removal and dipole inversion in a single iteration.
TIKH	Uses L2 regularization methods with closed form solutions.
TV	Uses minimized regularization term in the L1-norm to encourage sparsity.
RTS	Addresses the well-conditioned k-space using a Krylov subspace then solves the L1-minimization problem with no priori information.
TSVD/TKD	Uses a threshold to eliminates zero values from the k- space and substitutes them with small, non-zero values.

Varying the dipole inversion method while fixing the background field removal and 2) varying the background while fixing the dipole inversion methods. The background field removal and dipole inversion algorithms selected in this study are summarized in Table 3-1, which was explained in

detail in the literature review. Then, multiple assessments were used to evaluate the robustness of the used method which included two types of assessment: qualitative assessment and quantitative assessment. The qualitative assessment included a visual comparison between all methods across all patients, and the quantitative assessment included comparing the susceptibility values generated by these techniques in specific brain region that are relevant to HIE. We calculated the oxygenation levels (CSvO2) in the cerebral vein using the susceptibility of the surrounding tissue (mean susceptibility of the brain except the cerebral vein region). Finally, we compared these methods using two metrics: 1) white matter homogeneity which is defined by: one over the standard deviation of the susceptibility values and 2) veins contrast to evaluated QSM ability to reconstruct small structures, this metric was defined by: the maximum vein intensity over width of the vein. The non-parametric Wilcoxon signed-rank tests were applied to evaluate the potential statistical differences between methods for each quantitative evaluation metric. The method of Bonferroni correction was applied to correct for multiple comparisons.

3.1 Scientific publications

This work resulted in a conference publication at the Annual ISMRM conference 2022. In addition, an article has been submitted to "Magnetic Resonance Imaging" for publication. The manuscript is presented in Chapter 4 and is titled "Performance of background field removal and dipole inversion methods to reconstruct brain quantitative susceptibility mapping (QSM) data acquired in neonatal asphyxia". It presents the results that I obtained during my master's using different QSM algorithms.

CHAPTER 4 ARTCILE 1: PERFORMANCE OF BACKGROUND FIELD REMOVAL AND DIPOLE INVERSION METHODS TO RECONSTRUCT BRAIN QUANTITATIVE SUSCEPTIBILITY MAPPING (QSM) DATA ACQUIRED IN NEONATAL ASPHYXIA

Article submitted to Magnetic Resonance Imaging on December 19th, 2022

Title: Performance of background field removal and dipole inversion methods to reconstruct brain quantitative susceptibility mapping (QSM) data acquired in neonatal asphyxia

Daniel Ridani[1,2], Noée Ducros-Chabot[1,2], Mathieu Dehaes[2,3,*], Benjamin De Leener[1,2,4,*]

[1] NeuroPoly Lab, Institute of Biomedical Engineering, Polytechnique Montreal, Montreal, Qc, Canada

[2] Research Center, Sainte-Justine University Hospital Center, Montreal, Qc, Canada

[3] Department of Radiology, Radio-oncology, and Nuclear Medicine, University of Montreal, Montreal, Qc, Canada

[4] Department of Computer and Software Engineering, Polytechnique Montreal, Montréal Qc, Canada

[*] Equal contribution as co-senior authors

Contribution percentage: 80%

Abstract

Quantitative susceptibility mapping (QSM) recently gained popularity for being a biomarker for multiple diseases. Despite QSM's ability to quantify the human brain, it still faces many challenges, especially for neonates. The goal of this study is to compare several QSM reconstruction algorithm's performance to 16 patients following neonatal asphyxia and underwent therapeutic hypothermia, using different metrics and assessments such as: white matter homogeneity, venous contrast, Cerebral oxygen saturation ($CSvO_2$), and susceptibility values. We selected 7 different background field removal and 6 dipole inversion algorithms, and we made different combinations of them.

The results demonstrated that: (1) projection onto dipole (PDF) achieved the highest white matter homogeneity and Iterative Spherical Mean Value method (ISMV) achieved the highest venous contrast when varying the background field removal methods with fixed dipole inversion method (Rapid two step dipole (RTS)) and, (2) when varying the dipole inversion methods with fixed background field removal method (Regularization enabled sophisticated harmonic artefact reduction for phase data (RESHARP)), single-step total generalized variation (SSTGV) achieved the highest white matter homogeneity and Nonlinear dipole inversion (NDI) achieved the highest venous contrast. Susceptibility values and oxygenation levels agreed with previous QSM studies in the literature. This study provides background information on how to select the most appropriate QSM processing pipeline depending on the application.

Keywords

Magnetic resonance imaging (MRI); Quantitative susceptibility mapping (QSM); Dipole inversion; Background field removal; Cerebral venous oxygen saturation ($CSvO_2$); Neonates; Hypoxic ischemic encephalopathy (HIE).

4.1 INTRODUCTION

Neonatal hypoxic-ischemic encephalopathy (HIE) is a clinical syndrome of neurological dysfunction that occurs in 1.5 cases per 1000 live births [1]. The World Health Organization estimates that 8% of deaths of children under the age of 5 are due to HIE at birth [2]. Currently, hypothermia therapy, which consists of cooling patients for 72 h following the diagnostic of HIE, is the only treatment that shows a decrease in death [3]. While therapeutic hypothermia improves

survival rates and reduces severe neurodevelopmental disability, the incidence of brain injury and adverse neurodevelopmental outcomes is still high in this population [4].

Early markers of brain injury measured post-therapy may help to improve long-term outcome [5]. Among these markers, cerebral venous oxygen saturation (SvO_2), which is the quantity of unutilized oxygen in the veins after oxygen delivery and extraction by the brain, may be used to assess tissue viability and response to therapy. While cerebral SvO_2 are within 60-80% in stable neonates [6], altered values of cerebral SvO_2 may suggest the presence of brain injury [7]. Current gold standard techniques to measure cerebral SvO_2 are $^{15}O_2$ positron emission tomography [8] or through blood gas analysis, with blood sampled via a catheter inserted in the jugular vein. These techniques are invasive and less practical in neonates.

Magnetic resonance imaging (MRI) of the brain is clinically advised post-therapeutic hypothermia to detect brain injury. Quantitative susceptibility mapping (QSM) is an emerging MRI technique that uses the image phase signal from gradient echo data to determine the local tissue magnetic susceptibility [9]. QSM susceptibility maps combined with hematocrit in the blood allow one to quantify brain oxygenation through the calculation of cerebral SvO_2 [10]. Its potential for quantitative blood oxygenation measures has been shown in several studies. *Yadav et al* measured $CSvO_2$ in healthy fetuses using QSM (n=21, median gestational age (GA) 31.3 weeks). They reported a mean $CSvO_2$ of 67% (SD, 7%) [11]. In a similar study, *Weber et al* compared $CSvO_2$ between term (n=8, mean GA=40 weeks) and preterm neonates (n=8, mean GA=33.5 weeks) diagnosed with HIE and healthy controls (n=8, mean GA=39.3 weeks). They reported no significant difference between the groups, as they scored a mean $CSvO_2$ of 71.5% (SD, 7.4%), 72.2% (SD, 5.9%), 73.6% (SD, 2.8%), respectively [12]. While these studies hold great promises, current QSM image reconstruction methods were not developed for the developing brain, which may affect the quantification of oxygenation levels.

Additionally, the smaller brain structure and shorter acquisition time of the newborn can affect the quality of the images. QSM reconstruction pipelines typically consist of three major steps: (1) phase unwrapping: remove the discontinuity in phase by calculating the true phase value [13], (2) background field removal: isolate the field generated by local magnetic sources from the

background field induced by the variation in the susceptibility of surrounding tissue [14], and (3) dipole inversion: estimate the susceptibility of the brain and tissue oxygenation by solving the ill-posed field-to-source-inversion problem underlying QSM [15]. Several methods were proposed to achieve each of these steps and are detailed below. In this work, we implemented several QSM reconstruction algorithms and applied them to QSM data acquired in patients who underwent therapeutic hypothermia for HIE. We compared susceptibility values generated by these methods in specific brain regions and structures. We used susceptibility values from surrounding veins, including the external cerebral vein, internal cerebral vein, inferior sagittal sinus, and the straight sinus, to quantify cerebral SvO_2. We quantitatively compared these methods using two metrics: white matter homogeneity and venous contrast [16].

4.2 MATERIALS AND METHODS

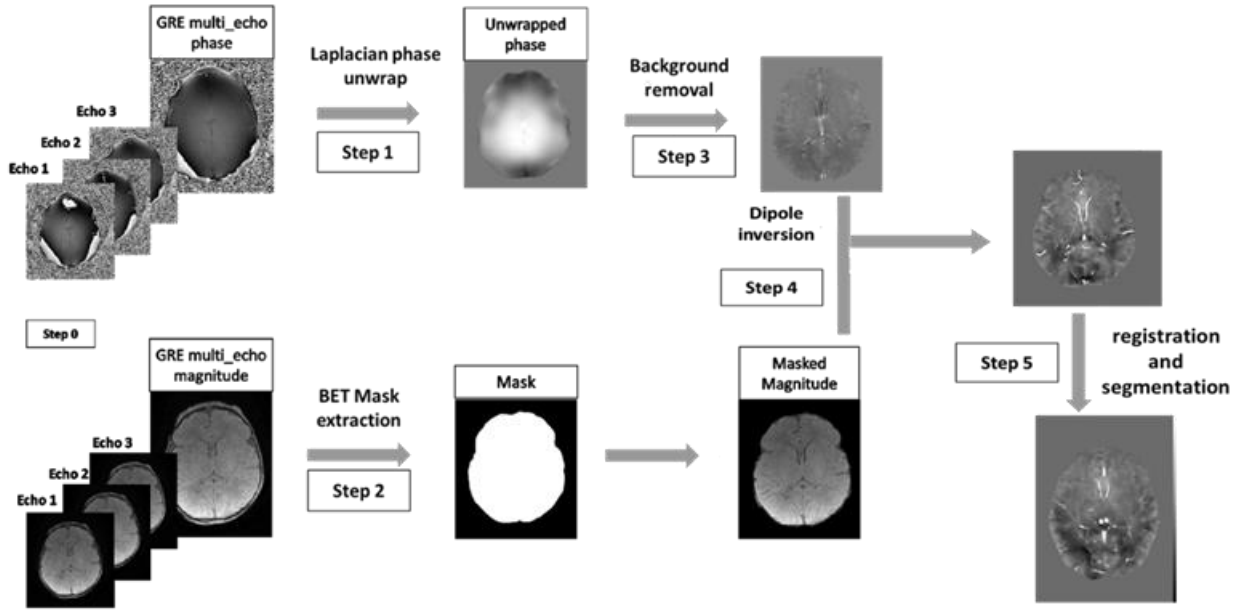

Figure 4-1: Diagram of the processing pipeline for QSM reconstruction used in this study, which includes: (0) data conversion to phase and magnitude images, (1) Laplacian phase unwrapping, (2) brain mask extraction, (3) background field removal, (4) dipole inversion and (5) registration to a generic template and segmentation of the brain regions (ex: white and gray matter).

4.2.1 Patients

This study was approved by the CHU Sainte-Justine Research Centre Ethics Committee for Human Experimentation. Sixteen (N=16) neonates undergoing hypothermia therapy for HIE who were

admitted at the CHU Sainte-Justine neonatal intensive care unit were included in this study. These patients were recruited within a larger study where inclusion/exclusion criteria are fully described [17]. Written informed consent was obtained from parents.

4.2.2 Clinical variables

Patient demographics and clinical variables were extracted from medical charts (Table 4-1). Hematocrit (HCT, %) was measured from the patient's blood sampled throughout the hospitalization using arterial blood gas analysis. HCT values measured at the closest timepoint relative to time of MRI were selected to quantify cerebral SvO_2.

4.2.3 MRI data acquisition

Neonates underwent post-therapy MRI between day 4 and discharge, with a median age of 6 days (IQ1=4.75, IQ3=6) in a 3T magnet (Discovery MR750, GE Healthcare, IL, USA). QSM data were acquired using a spoiled multi-echo gradient-echo (mGRE) sequence and a 32-channel head coil. Data acquisition was performed with a monopolar readout and flow compensation. Spatial resolution was 0.41x0.41x1.6 mm^3 and using the following parameters: Repetition time (TR) = 0.0207 s, Echo times (TEs) = 12, 15.38, and 18.76 ms, flip angle = 15°and field of view (FOV) = 20 cm.

Table 4-1: Demographic and clinical characteristics of neonates with HIE underwent therapeutic hypothermia. Data described as median (interquartile range, IQR), or number (%).

Clinical characteristic	HIE patients (N=16)
Gestational age, weeks	40.1 (38.2, 40.4)
Emergent Caesarian section	8 (50%)
Male sex	12 (75%)

Weight, kg	3.5 (3, 3.7)
Apgar scores, 5min	3.5 (2, 4)
Apgar scores, 10min	5.5 (3,6)
Umbilical artery pH or worst pH within the first hour	6.8 (6.7, 6.9)
Umbilical artery base excess or worst base excess within the first hour	17 (13.5, 19.8)
Resuscitation scores	3 (3, 4)
Age at full oral feed, days	6 (5,9)
Days on ventilator	5 (1, 6)
suspicion of clinical seizures	7 (44%)
Vasopressors	5 (31%)
Age at MRI, days	6 (5, 6)
Length of hospital stay	9 (6, 15)

4.2.4 Image reconstruction

Image reconstruction was performed using MATLAB 2021a (Natick, MA, USA) and included the following steps, as presented in Figure 4-1: (0) transformation of raw data into phase and magnitude images, (1) phase unwrapping, (2) brain masking and skull striping performed on the magnitude image using brain extraction tool (BET, FMRIB Software Library, UK) [18,19], (3) background field removal, (4) dipole inversion, and (5) co-registration of the susceptibility map to T1-weighted structural space specific for neonates [20] using a nonlinear registration method that uses an affine transformation to register two 3D volumes by maximization of their mutual information [21]. Using

a morphological atlas of the neonatal brain generated from data acquired at birth in healthy neonates born between 36 and 44 gestational weeks [22], susceptibility maps were segmented into specific structures, including white matter, thalamus, caudate nucleus, and deep grey matter. Several of these steps are detailed in the sections below.

To evaluate our capabilities to properly reconstruct susceptibility maps from mGRE data, we evaluated the following methods for two of the most important reconstruction steps: background field removal and dipole inversion. For these comparisons, the Laplacian phase unwrapping method was used in the first step due to its fast execution time and its stable results [23]. The Laplacian phase unwrap algorithms unwrap the phase image by solving the Laplacian operator. The Laplacian is computed by taking the second derivative of the phase data in both the x and y directions.

For step 2, we selected the following methods for background field removal: projection onto dipole fields (PDF) [24], iterative spherical mean value method (ISMV) [25], Laplacian boundary value (LBV) [26], regularization enabled sophisticated harmonic artifact reduction for phase (RESHARP) [27], variable sophisticated harmonic artifact reduction for phase (VSHARP) [13, 28], and sophisticated harmonic artifact reduction for phase (SHARP) [29]. To compute the final susceptibility maps, tissue phase images obtained using the above algorithms were further processed using the rapid two-step dipole inversion with sparsity priors (RTS) method [30]. This dipole inversion method was selected due to its better visual quality of the reconstructed QSM and relatively better computational efficiency.

The third step is to apply dipole inversion. We selected eight dipole inversion techniques and applied them after background removal: morphology enabled dipole inversion (MEDI) [31], nonlinear dipole inversion (NDI) [32], single-step total generalized variation (SSTGV) [33], Tikhonov regularization (TIKH) [34], truncated k-space division (TKD) [35], truncated singular value decomposition (TSVD) [36], total variation deconvolution (TV) [37], and RTS: rapid two-step dipole inversion with sparsity priors [30]. To compare these methods, we selected the RESHARP method for background removal due to its stability to estimate the background field [38].

4.2.5 QSM assessment metrics

To compare the reconstruction algorithms described above, we performed a qualitative comparison and used two quantitative metrics that have been used in the literature: (1) white matter homogeneity and (2) venous contrast. Additionally, we computed the cerebral SvO_2 and extracted the susceptibility values in several brain regions and compared them to the literature.

White matter homogeneity: For each patient, white matter homogeneity was calculated as one over the standard deviation of the susceptibility values of the white matter tissue mask obtained after co-registration in the age-appropriate neonatal template (see Figure 4-2 A) [21, 22]. This metric provides a proxy measure of residual background phase and low-frequency artifacts. This metric can be used to quantify the robustness of the method by representing the residual background phase, which should be minimal [16].

Venous contrast: Veins have high susceptibility values due to their rich content in deoxyhemoglobin. To measure venous contrast, we performed a line profile through transverse sections of the same vein for each patient. Venous contrast was defined as the maximum susceptibility in the vein profile divided by the full width half maximum (FWHM) value (see Figure 4-2 B). Venous contrast was normalized by considering the vein width (which may vary between patients). This normalization allowed us to compare venous contrast between patients. The normalization is defined by the following expression:

$$FWHM_{normilazed} = \frac{FWHM - FWHM_{minimum}}{FWHM_{maximum} - FWHM_{minimum}}$$

The higher the contrast is, the is easier to distinguish it from the surrounding tissue [51].

Cerebral SvO_2: This metric is computed in the cerebral veins (red mask in Figure 4-2 C) by thresholding out 99.995% of the lower magnetic susceptibility value. Cerebral SvO_2 was then calculated in the cerebral veins using the following formula:

$$\Delta\chi = \Delta\chi_{do} \times HCT \times (1 - CSvO_2)$$

Where $\Delta\chi$ is the susceptibility difference between venous blood and the surrounding tissue, which is defined by the mean susceptibility of the brain except the cerebral vein region, $\Delta\chi_{do}$ is the susceptibility shift per unit of hematocrit between fully oxygenated and fully deoxygenated blood and assumed to be 0.27 ppm [10, 39], and HCT is the individual hematocrit.

Susceptibility in brain regions and structures: Regions and structures were determined by segmentation of susceptibility maps in the age-appropriate neonatal template [22] and included: the thalamus, deep gray nuclei, caudate nucleus, and white matter since they are the region that might be most affected by HIE [40]. Susceptibility values for other regions are included in the supplementary materials.

Non-parametric Wilcoxon signed-rank tests, corrected for multiple comparison using the Bonferroni correction method, were used to evaluate the potential statistical differences between the methods for each quantitative evaluation metric.

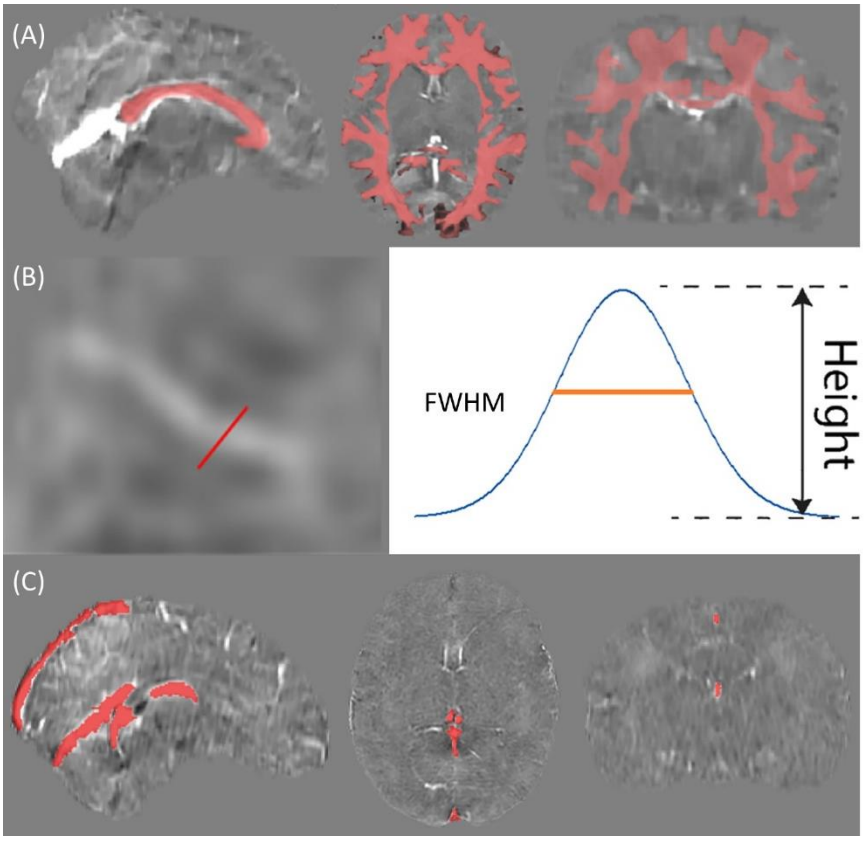

Figure 4-2: A. The mask used to extract the white matter across the brain. B. An example of line profile perpendicular the vein shown in the image on the left and on the right the definition of the max height and the FWHM. C. Regions where the oxygenation was extracted in the cerebral vein after 99.995% thresholding.

4.3 RESULTS

4.3.1 Qualitative assessment

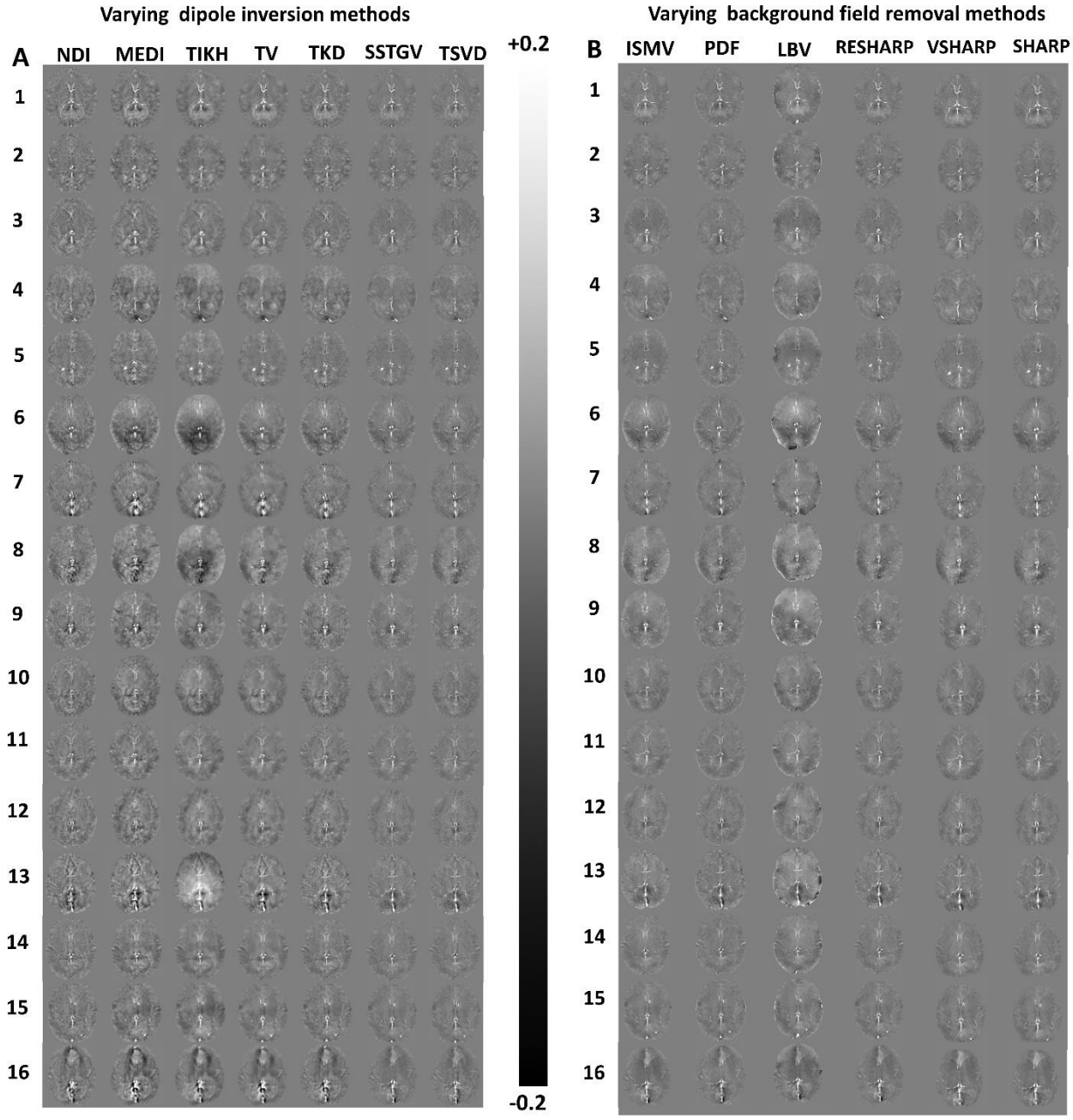

Figure 4-3*: Visual comparison of susceptibility maps reconstructed from the (A) combination of the background field removal method RESHARP with dipole inversions methods (NDI, MEDI, TIKH, TV, TKD, SSTGV, and TSVD). (B) combination of background field removal methods (ISMV, PDF, LBV, RESHARP, VSHARP, and SHARP) with the dipole inversion method RTS. Each reconstruction was applied to each patient.*

Figure 3 presents a visual comparison of susceptibility maps generated by the combinations of background field removal and dipole inversion methods described above. We can observe that some patients (patient 6, 8, 13) show more signal dropouts and hyperintensities than others using the same exact method. When varying the background field removal method (Figure 4-3 A), LBV shows signal hyperintensities located in posterior regions of the brain, while the other methods show consistent maps. MEDI and TIKH dipole inversion methods appear to increase the image contrast as well as signal dropouts and hyperintensities, while SSTGV and TSVD provide more homogeneous images (Figure 4-3 B). Qualitatively, varying the background field removal method results in more homogeneous and consistent susceptibility maps than varying the dipole inversion method.

4.3.2 Quantitative assessment

4.3.3 White matter homogeneity

Figure 4-4 A presents the distributions of white matter homogeneity across the entire cohort when varying the background field removal method for a fixed dipole inversion technique (RTS) while Figure 4-4 B shows results when varying dipole inversion algorithms with a fixed background removal method (RESHARP). Among the dipole inversion methods, SSTGV had the highest white matter homogeneity compared to MEDI, which had the lowest homogeneity. Among all the background field removal methods, PDF had the highest white matter homogeneity, while LBV had the lowest white matter homogeneity.

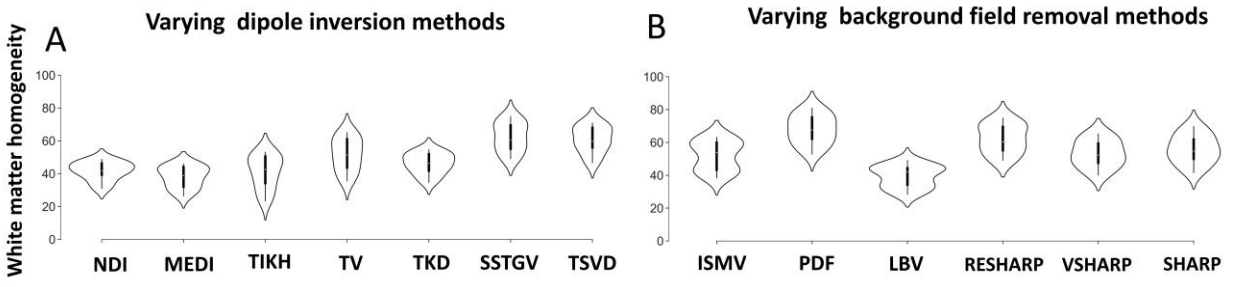

Figure 4-4: White matter homogeneity across the entire cohort when varying (A) the background field removal for a fixed dipole inversion method (RTS) and (B) the dipole inversion methods with a fixed background field removal method (RESHARP)

4.3.4 Venous contrast

Figure 4-5 A presents the distributions of venous contrast metric across the entire cohort when varying the dipole inversion method for a fixed background field removal technique (RESHARP) while Figure 4-5 B shows results when varying background field removal algorithms with a fixed dipole inversion method (RTS). The plot shows that NDI showed the highest venous contrast, while TIKH had the lowest value. Among the background field removal methods, ISMV provided the highest venous contrast, while LBV got the lowest value. Figure 5 C shows the location of the vein used for metric calculation and a visual comparison of the venous contrast for one patient for both background field removal and dipole inversion methods.

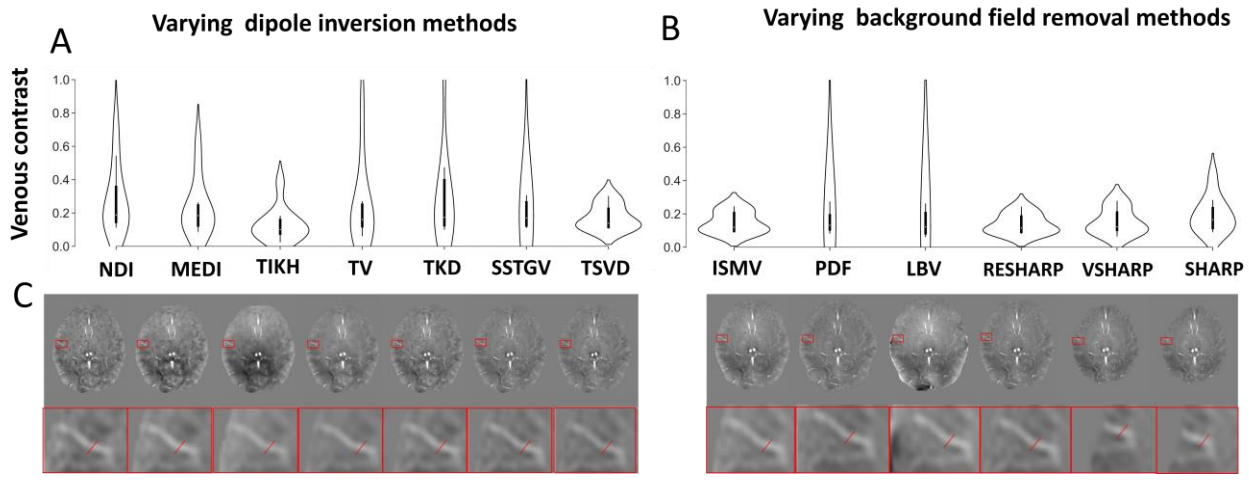

Figure 4-5: Venous contrast across the entire cohort when varying (A) the dipole inversion methods with a fixed background field removal method (RESHARP) and (B) the background field removal for a fixed dipole inversion method (RTS) (C) visual representation of the veins.

4.3.5 $CSvO_2$ levels

Figure 4-6 presents the distribution of (A) cerebral SvO_2 across the entire cohort when varying the dipole inversion method for a fixed dipole inversion technique (RESHARP) while (B) shows results when varying background field removal algorithms with a fixed dipole inversion method (RST). Correspondingly, the mean $CSvO_2$ values were 73.7%(SD=6.64%) and 74.4%(SD=5.52%) for dipole inversion and background field removal methods respectively.

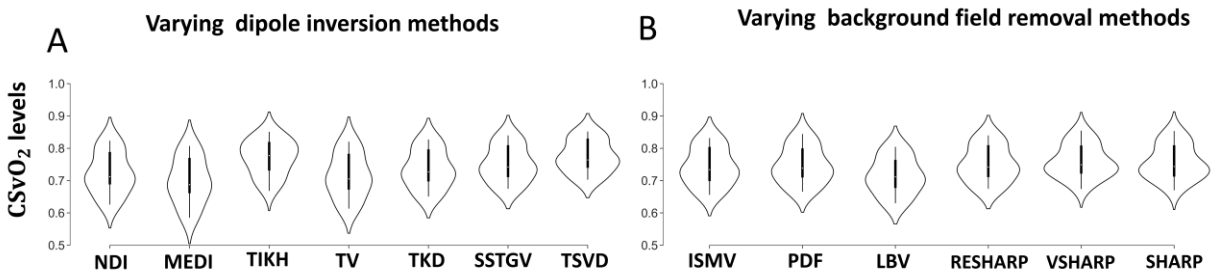

Figure 4-6: Cerebral SvO_2 across the entire cohort when varying (A) the dipole inversion methods with a fixed background field removal method (RESHARP) and (B) the background field removal for a fixed dipole inversion method (RTS).

4.3.6 Susceptibility values

Figure 4-7 shows the distributions of averaged susceptibility maps for each patient and for four cerebral regions: white matter, deep grey matter, the caudate nucleus, and the thalamus. These regions were selected as examples due to a higher incidence of brain injury in these regions in neonates with HIE. Average susceptibility values across all patients in the remaining brain regions (14 region) are presented in Supplementary Table 2. Figure 7 A shows susceptibility distributions when varying the dipole inversion method for a fixed background field removal technique (RESHARP) while Figure 7 B shows results when varying background field removal algorithms with a fixed dipole inversion method (RST). TIKH showed more variability among the dipole inversion methods. When comparing the background field removal methods, LBV showed more variability in the deep structures (excluding white matter).

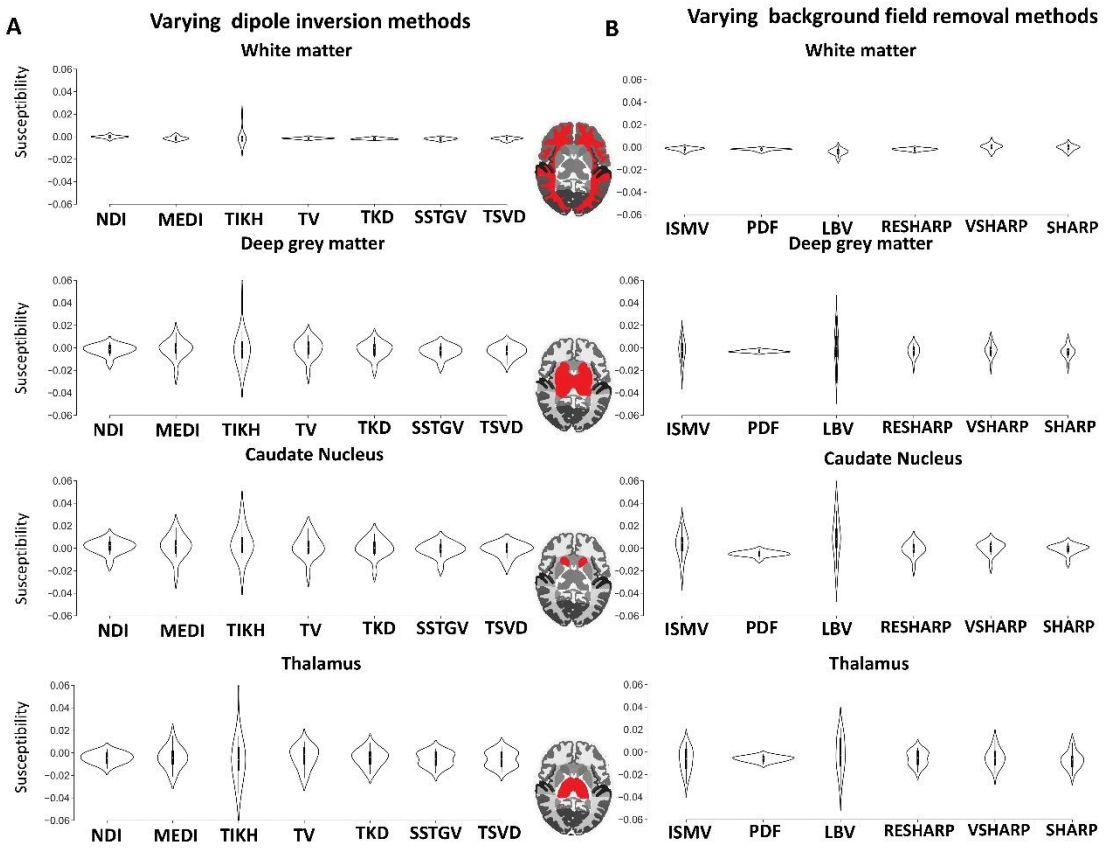

Figure 4-7: Susceptibility values for different parts of the brain across the entire cohort when varying. (A) the dipole inversion methods with a fixed background field removal method (RESHARP) and (B) the background field removal for a fixed dipole inversion method (RTS). The brain images between panels A and B show the masks used for extraction in each region of interest.

4.3.7 Statistical comparison between methods

When looking for statistical differences between methods for each metric, we performed Wilcoxon parametric tests between each pair of methods and corrected for multiple comparisons using Bonferroni correction methods (N=21 for dipole inversion methods and N=15 for background field removal). Results show that when comparing methods on white matter homogeneity, (1) for dipole inversion, all methods showed to be significantly different from each other except between NDI and TIKH and between MEDI and TIKH; (2) for background field removal, all methods were statically different except between ISMV and VSHARP. When looking at the venous contrast, we did not observe any statical difference between methods for any of the two steps. Finally, we did not observe any statistical difference between methods for dipole inversion when looking at $CSvO_2$

and we observe a statistical difference between all methods for background field removal, except between ISMV/PDF, PDF/SHARP, RESHARP/VSHARP, and RESHARP/ VSHARP combinations.

4.4 DISCUSSION

To our knowledge, this study is the first to assess the performance of several background field removal and dipole inversion methods to reconstruct cerebral QSM data acquired in neonates undergoing therapeutic hypothermia for HIE. QSM data can be used to derive cerebral SvO_2, which may aid in detecting early brain injury and further improve long-term outcomes. Our study demonstrates that the various methods that we implemented and compared provided different results, but their interpretation can be difficult. Accordingly, to ensure optimal results, QSM processing strategies should be carefully selected based on the question of interest. QSM maps were judged based on a qualitative and quantitative assessment which included four metrics across all the cohorts: (1) white matter homogeneity metric assumes that the white matter should be homogeneous if the algorithm is robust: low homogeneity is a probable sign of low spatial frequency artifacts or more residual background phase components. Although few studies suggested the heterogenous nature of white matter for adults [41], neonates are still in the first stages of development, which led us to believe that the assumption of homogeneity is valid. The venous contrast metric ensures that the method can reliably reconstruct QSM in small structures with high susceptibility values. Extracting the susceptibility values in four regions of interest of the neonatal brain allowed us to compare the QSM values across the brain in relation to the question of interest. Finally, calculating the cerebral SvO_2 allows us to compare the various QSM reconstruction methods to values found in the literature (acquired invasively or non-invasively). The next paragraphs will discuss the results and their limitations.

First, we analyzed the results obtained by varying the dipole inversion method with fixed background field removal methods (RESHARP). This algorithm was selected based on five reasons: 1) its stability and homogeneity in estimating the background field across the entire cohort [42], 2) a better visual quality of reconstructed QSM, 3) it incorporates a Tikhonov regularization that may suppress the residual background field into the deconvolution [27], 4) it produces reliable

results close to boundaries compared to other methods [27], 5) fast computing time [42]. MEDI showed poor results for white matter homogeneity and high variability in computing the susceptibility, which indicates potential instability for the computation of the susceptibility across the population. Despite the simultaneous regional blurring that is typical of this approach, this instability was also reported by *Yicheng Chen et al* for both 3T and 7T MRI [16]. A possible explanation for this instability is the fact that this technique is more sensitive to the regularization parameters, in addition to the signal dropout or/and hyperintensities associated with this reconstruction method in the ROI. Venous contrast showed significant differences among all the reconstruction methods, which indicated the importance of choosing the optimal methods for specific applications of interest that are required to extract susceptibility-related measures within these structures. Our results demonstrated that NDI and TKD have the highest contrasted and sharp veins, which is encouraging for the use of quantitative susceptibility mapping in the neonatal brain, while TIKH scored the lowest for this metric. We believe that the regularization terms in these methods, when not defined properly, could make the reconstructed images appear blurrier. Blurrier images limit the ability to identify boundaries between different regions, which then will make the veins wider and the contrast values lower. It has to be noted that we did not explore the full range of possible parameters for each method, including balancing the regularization terms within their optimization function.

Second, we analyzed the same metrics and assessment, while varying the background field removal methods and fixing the dipole inversion method (RTS). The RTS algorithm was selected for three main reasons: 1) better visual quality of QSM, 2) *Christian Kames et al*. reported a lower mean-square error with respect to COSMOS compared to other techniques, and 3) faster computation time [30]. LBV showed the lowest white matter homogeneity, but the lowest venous contrast compared to other background field removal methods used. In addition, LBV showed an important variability in terms of susceptibility values, especially in the deep structure of the brain (except for white matter), across the population. However, it showed apparent errors close to the brain boundary. *Xuanyu Zhu et al*. reported that LBV displayed the highest measurement variation and apparent residual background field compared to other background field removal techniques [43].

In general, when varying the dipole inversion methods or varying the background field removal methods, susceptibility values agreed with the literature, although these values were lower than the susceptibility values in adults. While we are not able to compare healthy neonates with healthy adults in this study, this age-dependent effect is expected since the neonatal brain is still developing. Indeed, iron and myelin concentrations are much lower in the neonatal brain compared to the adult brain, resulting in lower susceptibility values. *Yuyao Zhang et al*. studied brain development from birth to 2 years using QSM and compared the results to a group of healthy adults who reported significant differences in susceptibility values between age groups [44].

Finally, we analyzed the $CSvO_2$ levels for all the patients. This metric could be used as a potential early biomarker of brain injury. *Chao Chai et al* reported the importance of cerebral SvO_2 as a biomarker for brain function and that it could be used to monitor patient progress [45]. In our results, we observed comparable values with other studies that extracted $CSvO_2$ levels using QSM [11, 12]. Almost all the values were in the normal range: between 60% and 80%. To improve the accuracy of the metric, other studies in the literature have suggested measuring the cerebral SvO_2 using an invasive method such as jugular venous oxygen saturation ($SjvO_2$), which is considered giving accurate results but comes with a risk of damaging the body [46], or with other non-invasive methods such near infrared resonance spectroscopy (NIRS), which has been shown to have poor sensitivity at low $CSvO_2$ [47]. The QSM-based non-invasive technique presented in this manuscript may be a potential replacement for existing invasive and non-invasive methods to estimate brain oxygenation. As this metric is based on a fast acquisition sequence, it may even be clinically feasible. Future research is needed to better understand the QSM signals in neonatal HIE for clinical implementation.

Although this study was the first to compare QSM reconstruction methods for neonates, there were several limitations: 1) the lack of healthy controls makes any comparison difficult when looking at the susceptibility and $CSvO_2$ values. 2) Although the COSMOS technique is considered by some as the gold standard for susceptibility mapping, this technique is difficult to implement in neonates, as it requires rotating the region of interest within the scanner and acquiring multiple images, thus increasing the acquisition time. For this reason, it may be difficult to compare QSM reconstruction methods appropriately, without knowing the true value of the susceptibility of the tissues. 3) Our

QSM sequences were based on three echoes, while other studies reported QSM reconstructions with more than 6 echoes. Three echoes were selected as a good compromise for decreasing the acquisition time while ensuring good quality data. Future studies should explore new ways of acquiring high-quality images for QSM reconstruction. 4) We used a single threshold to identify the cerebral venous region, while there might be various optimal thresholds of another approach that would perform better across the population. 5) The study lacks an association between QSM data (susceptibility and cerebral SvO2) and a short-term (clinical MRI) or long-term outcome (neurodevelopmental scores).

4.5 CONCLUSION

Quantitative susceptibility mapping of the neonatal brain is a challenging task [48]. This study compared various QSM reconstruction algorithms by using different combinations of background field removal and dipole inversion methods in a neonatal population who was diagnosed with hypoxic-ischemic encephalopathy. The results demonstrated robust QSM values in the neonatal brain, as shown by apparent small structures such as blood vessels.

The results of this work can be summarized as the following: PDF and SSTGV achieved the highest white matter homogeneity for background field removal and dipole inversion respectively, ISMV and NDI scored the highest venous contrast for background field removal; methods and dipole inversion methods respectively, Susceptibility values were similar to reported values in the literature, and we showed comparable $CSvO_2$ levels to the literature (oxygenation) for the explored methods. Future work will include the development of new algorithms that are suited for the neonatal brain, for example taking into consideration the differences in tissue microstructure between the neonate and the adult brain. These aspects will help to select the most appropriate method in terms of reliability, reproducibility, speed, and efficiency and push the boundaries of our understanding of HIE. Meanwhile, our results could be considered a guide for selecting the most appropriate reconstruction methods for future research on QSM data in the neonatal brain.

Code availability

The QSM algorithm as well as the registration, segmentation and metrics calculation can be freely accessed at: https://github.com/Danirid/QSM-HIE

Declaration of Competing Interest

None.

4.6 ACKNOWLEDGMENTS

This study was supported by Polytechnique Montréal, by the Canada First Research Excellence Fund, by the TransMedTech Institute and by the Canadian Institutes of Health Research. We also would like to thank the newborn's families who agreed to be part of this study as well as the medical staff who helped collected the data. Without them, this study would not be possible.

4.7 REFERENCES

1. Kurinczuk, J.J., M. White-Koning, and N. Badawi, *Epidemiology of neonatal encephalopathy and hypoxic–ischaemic encephalopathy*. Early human development, 2010. **86**(6): p. 329-338.
2. Bryce, J., et al., *WHO estimates of the causes of death in children.* The lancet, 2005. **365**(9465): p. 1147-1152.
3. Shankaran, S. and A.R. Laptook, *Hypothermia as a treatment for birth asphyxia.* Clinical obstetrics and gynecology, 2007. **50**(3): p. 624-635.
4. Jacobs, S., et al., *Cooling for newborns with hypoxic ischaemic encephalopathy*. Pediatric Research, 2005. **58**(2): p. 385.
5. Rutherford, M., et al., *Hypoxic-ischaemic encephalopathy: early and late magnetic resonance imaging findings in relation to outcome.* Archives of Disease in Childhood-Fetal and Neonatal Edition, 1996. **75**(3): p. F145-F151.
6. van der Hoeven, M.A., W.J. Maertzdorf, and C.E. Blanco, *Continuous central venous oxygen saturation (ScvO2) measurement using a fibre optic catheter in newborn infants.* Archives of Disease in Childhood-Fetal and Neonatal Edition, 1996. **74**(3): p. F177-F181.
7. van Beest, P., et al., *Clinical review: use of venous oxygen saturations as a goal-a yet unfinished puzzle.* Critical Care, 2011. **15**(5): p. 1-9.
8. Cumming, P., *PET neuroimaging: the white elephant packs his trunk?* Neuroimage, 2013. **84**: p. 1094-1100.
9. Haacke, E.M., et al., *Quantitative susceptibility mapping: current status and future directions.* Magnetic resonance imaging, 2015. **33**(1): p. 1-25.

10. Weisskoff, R.M. and S. Kiihne, *MRI susceptometry: image-based measurement of absolute susceptibility of MR contrast agents and human blood.* Magnetic resonance in medicine, 1992. **24**(2): p. 375-383.

11. Yadav, B.K., et al., *Quantitative susceptibility mapping in the human fetus to measure blood oxygenation in the superior sagittal sinus*. European radiology, 2019. **29**(4): p. 2017-2026.

12. Weber, A., et al., *Quantitative Susceptibility Mapping of Venous Vessels in Neonates with Perinatal Asphyxia.* American Journal of Neuroradiology, 2021. **42**(7): p. 1327-1333.

13. Li, W., B. Wu, and C. Liu, *Quantitative susceptibility mapping of human brain reflects spatial variation in tissue composition.* Neuroimage, 2011. **55**(4): p. 1645-1656.

14. Schweser, F., et al., *An illustrated comparison of processing methods for phase MRI and QSM: removal of background field contributions from sources outside the region of interest.* NMR in Biomedicine, 2017. **30**(4): p. e3604.

15. Schweser, F., A. Deistung, and J.R. Reichenbach, *Foundations of MRI phase imaging and processing for Quantitative Susceptibility Mapping (QSM).* Zeitschrift für medizinische Physik, 2016. **26**(1): p. 6-34.

16. Chen, Y., et al., *Comparison of quantitative susceptibility mapping methods on evaluating radiation-induced cerebral microbleeds and basal ganglia at 3T and 7T.* NMR in Biomedicine, 2022. **35**(5): p. e4666.

17. Mahdi, Z., et al., *Opioid analgesia and temperature regulation are associated with EEG background activity and MRI outcomes in neonates with mild-to-moderate hypoxic-ischemic encephalopathy undergoing therapeutic hypothermia.* European Journal of Paediatric Neurology, 2022. **39**: p. 11-18.

18. Smith, S.M., et al., *Advances in functional and structural MR image analysis and implementation as FSL.* Neuroimage, 2004. **23**: p. S208-S219.

19. Smith, S.M., *Fast robust automated brain extraction.* Human brain mapping, 2002. **17**(3): p. 143-155.

20. Avants, B.B., N. Tustison, and G. Song, *Advanced normalization tools (ANTS).* Insight j, 2009. **2**(365): p. 1-35.

21. Mattes, D., et al., *PET-CT image registration in the chest using free-form deformations.* IEEE transactions on medical imaging, 2003. **22**(1): p. 120-128.

22. Schuh, A., et al., *Unbiased construction of a temporally consistent morphological atlas of neonatal brain development.* BioRxiv, 2018: p. 251512.

23. Schofield, M.A. and Y. Zhu, *Fast phase unwrapping algorithm for interferometric applications.* Optics letters, 2003. **28**(14): p. 1194-1196.

24. Liu, T., et al., *A novel background field removal method for MRI using projection onto dipole fields.* NMR in Biomedicine, 2011. **24**(9): p. 1129-1136.

25. Wen, Y., et al., *An iterative spherical mean value method for background field removal in MRI.* Magnetic resonance in medicine, 2014. **72**(4): p. 1065-1071.

26. Zhou, D., et al., *Background field removal by solving the Laplacian boundary value problem.* NMR in Biomedicine, 2014. **27**(3): p. 312-319.

27. Sun, H. and A.H. Wilman, *Background field removal using spherical mean value filtering and Tikhonov regularization.* Magnetic resonance in medicine, 2014. **71**(3): p. 1151-1157.

28. Wu, B., et al., *Whole brain susceptibility mapping using compressed sensing.* Magnetic resonance in medicine, 2012. **67**(1): p. 137-147.

29. Schweser, F., et al., *Quantitative imaging of intrinsic magnetic tissue properties using MRI signal phase: an approach to in vivo brain iron metabolism?* Neuroimage, 2011. **54**(4): p. 2789-2807.

30. Kames, C., V. Wiggermann, and A. Rauscher, *Rapid two-step dipole inversion for susceptibility mapping with sparsity priors.* Neuroimage, 2018. **167**: p. 276-283.

31. Liu, J., et al., *Morphology enabled dipole inversion for quantitative susceptibility mapping using structural consistency between the magnitude image and the susceptibility map.* Neuroimage, 2012. **59**(3): p. 2560-2568.

32. Polak, D., et al., *Nonlinear dipole inversion (NDI) enables robust quantitative susceptibility mapping (QSM).* NMR in Biomedicine, 2020. **33**(12): p. e4271.

33. Langkammer, C., et al., *Fast quantitative susceptibility mapping using 3D EPI and total generalized variation.* Neuroimage, 2015. **111**: p. 622-630.

34. Bilgic, B., et al., *Fast image reconstruction with L2-regularization.* Journal of magnetic resonance imaging, 2014. **40**(1): p. 181-191.

35. Shmueli, K., et al., *Magnetic susceptibility mapping of brain tissue in vivo using MRI phase data.* Magnetic Resonance in Medicine: An Official Journal of the International Society for Magnetic Resonance in Medicine, 2009. **62**(6): p. 1510-1522.

36. Wharton, S., A. Schäfer, and R. Bowtell, *Susceptibility mapping in the human brain using threshold-based k-space division.* Magnetic resonance in medicine, 2010. **63**(5): p. 1292-1304.

37. Blomgren, P. and T.F. Chan, *Color TV: total variation methods for restoration of vector-valued images.* IEEE transactions on image processing, 1998. **7**(3): p. 304-309.

38. Kan, H., et al., *Background field removal technique using regularization enabled sophisticated harmonic artifact reduction for phase data with varying kernel sizes.* Magnetic Resonance Imaging, 2016. **34**(7): p. 1026-1033.

39. Sedlacik, J., A. Rauscher, and J.R. Reichenbach, *Obtaining blood oxygenation levels from MR signal behavior in the presence of single venous vessels.* Magnetic Resonance in Medicine: An Official Journal of the International Society for Magnetic Resonance in Medicine, 2007. **58**(5): p. 1035-1044.

40. Allen, K.A. and D.H. Brandon, *Hypoxic ischemic encephalopathy: pathophysiology and experimental treatments.* Newborn and Infant Nursing Reviews, 2011. **11**(3): p. 125-133.

41. Li, T.Q., et al., *Characterization of T2* heterogeneity in human brain white matter.* Magnetic Resonance in Medicine: An Official Journal of the International Society for Magnetic Resonance in Medicine, 2009. **62**(6): p. 1652-1657.

42. Fang, J., et al., *Background field removal using a region adaptive kernel for quantitative susceptibility mapping of human brain.* Journal of Magnetic Resonance, 2017. **281**: p. 130-140.

43. Zhu, X., et al., *BFRnet: A deep learning-based MR background field removal method for QSM of the brain containing significant pathological susceptibility sources.* arXiv preprint arXiv:2204.02760, 2022.

44. Zhang, Y., et al., *Neonate and infant brain development from birth to 2 years assessed using MRI-based quantitative susceptibility mapping.* Neuroimage, 2019. **185**: p. 349-360.

45. Chai, C., et al., *Decreased susceptibility of major veins in mild traumatic brain injury is correlated with post-concussive symptoms: a quantitative susceptibility mapping study.* Neuroimage: clinical, 2017. **15**: p. 625-632.

46. Zhong, W., Z. Ji, and C. Sun. *A Review of Monitoring Methods for Cerebral Blood Oxygen Saturation*. in *Healthcare*. 2021. MDPI.

47. Rescoe, E., et al., *Cerebral near-infrared spectroscopy insensitively detects low cerebral venous oxygen saturations after stage 1 palliation.* The Journal of thoracic and cardiovascular surgery, 2017. **154**(3): p. 1056-1062.

48. Dubois, J., et al., *MRI of the neonatal brain: a review of methodological challenges and neuroscientific advances.* Journal of Magnetic Resonance Imaging, 2021. **53**(5): p. 1318-1343.

CHAPTER 5 GENERAL DISCUSSION

In this chapter, I will be discussing the methods used in this project and the results that were presented in Chapter 4.

5.1 QSM image reconstruction

According to our knowledge, this work is the first to evaluate how well various background field removal and dipole inversion algorithms perform when used to rebuild cerebral QSM data obtained from 16 infants who were receiving therapeutic hypothermia for HIE. Cerebral SvO2 can be derived from QSM data, which may help to identify brain injury early and to enhance long-term outcomes. Our study reveals that the diverse approaches we used and compared had varying outcomes, and their interpretation can be challenging. Therefore, based on the question of interest, QSM processing algorithms should be carefully chosen to achieve the best outcomes. QSM maps were evaluated using both qualitative and quantitative methods. Four metrics were used to assess the maps across the entire cohort: white matter homogeneity, venous contrast, susceptibility values in four brain regions, and cerebral SvO2. The white matter homogeneity metric was used to ensure that the algorithm was robust, and that low homogeneity was not a result of low spatial frequency artifacts or residual background phase components. Venous contrast was used to test the technique's reliability in reconstructing regions with high susceptibility values. Susceptibility values in four brain regions were used to compare the accuracy of QSM reconstruction in computing susceptibility. Finally, cerebral SvO2 was compared to other existing methods (invasive or non-invasive). It is worth noting that while some studies have suggested that the white matter may be heterogeneous in adults, neonates are still in the early stages of development, leading us to believe that the assumption of homogeneity is valid in this case [52].

5.2 Evaluation metrics

5.2.1 Dipole inversion methods

In this study, the RESHARP algorithm was selected for analyzing the results of varying the dipole inversion method with fixed background field removal methods. RESHARP was chosen due to its stability, homogeneity, visual quality, regularization, reliability near boundaries, and fast

computing time [53]. The results came as follows: MEDI had poor results for white matter homogeneity and susceptibility computation variability, indicating potential instability for susceptibility computation across the cohort. Venous contrast showed significant differences among the techniques, with NDI and TKD performing the best for use in neonatal brain QSM. TIKH had lower performance, possibly due to regularization terms that made the images blurrier.

5.2.2 Background field removal methods

In our analysis, we also evaluated the performance of different background field removal methods using a fixed dipole inversion method (RTS). We selected the RTS algorithm for its improved visual quality, lower mean-square error compared to COSMOS (as reported by Christian Kames *et al*), and faster computation time. Among the background field removal methods we tested, LBV had the lowest white matter homogeneity and venous contrast. Due to interpolations caused by the violin plot, a value cutoff at zero was imposed, to exclude any negative values, to ensure that only positive values are used in the analysis and eliminate any confusion about the presence of negative values.

LBV also exhibited significant errors near brain boundaries. This may be due to the assumption of a uniform background field throughout the boundary region. Previous research by Xuanyu Zhu *et al* has also confirmed that LBV had the highest measurement variation compared to other background field removal techniques [54].

5.3 Susceptibility values for neonates

Both methods (varying the dipole inversion method and varying the background field removal method) produced susceptibility values that were consistent with previous research, although these values were different from those found in adult brains, as expected due to the ongoing development of the neonatal brain. Iron and myelin are the two main sources of susceptibility in the brain, where iron has a positive susceptibility (paramagnetic) and myelin has a negative susceptibility (diamagnetic). In addition, the neonatal brain is in constant development, and it does not complete full myelination until around age 25. Thus, the neonatal brain has lower iron and myelin concentrations than the adult brain, resulting in lower susceptibility values in area dominated by

iron and higher susceptibility values in area dominated by myelin. *Yuyao Zhang et al* study on brain development from birth to 2 years using QSM and comparison to a group of healthy adults found significant differences in susceptibility values between the ages [55].

5.4 Cerebral venous oxygen saturation ($CSvO_2$)

In this study, cerebral SvO2 levels were analyzed as a potential early marker of brain injury [56]. The results showed that these levels were within the normal healthy range and were consistent with other studies that used QSM to measure cerebral SvO2. Other methods for measuring cerebral SvO2, such as invasive jugular venous oxygen saturation monitoring and non-invasive near infrared resonance spectroscopy, have limitations that our non-invasive QSM technique may be able to overcome. Further research is needed to understand the use of QSM in neonatal HIE for clinical implementation.

5.5 Limitations

This study compared QSM reconstruction methods for neonates and had several limitations. First, the lack of healthy controls made it difficult to compare susceptibility and cerebral SvO2 values. Second, the low sample size. Third, the QSM sequences in this study were based on 3 TEs, while other studies used more, which may have affected image quality. Fourth, using the same threshold to identify the cerebral venous region may not have been appropriate for datasets with different signal intensity ranges. Finally, there was no association between QSM data (susceptibility and cerebral SvO2) and short-term (clinical MRI) or long-term (neurodevelopmental scores) outcomes.

CHAPTER 6 CONCLUSION AND RECOMMENDATIONS

6.1 Conclusion

This thesis investigated the feasibility of quantitative susceptibility mapping (QSM) in neonates diagnosed with HIE and who underwent hypothermia. We compared multiple QSM algorithms in order to see which one is the more suitable.

Chapter 5 focused on the QSM reconstruction pipeline that was used to study two major steps in QSM reconstruction: background field removal and dipole inversion. This chapter evaluated and compared these algorithms in a qualitative approach as well as a quantitative approach using multiple metrics such as veins contrast and white matter homogeneity for neonates with HIE. The findings of this study emphasize the significance of picking a QSM processing technique carefully based on the question of interest, since, for example, susceptibility values can change depending on the technique chosen for background field removal and dipole inversion.

6.2 Recommendations

Quantitative susceptibility mapping for neonates is still a big research interest for many researchers.. The next step would be to expand the quality evaluation metrics to precisely compare all the reconstruction algorithms in order to establish a golden standard. In addition, the development of new algorithms that are suited to neonates and take into consideration anatomy differences like the size of the brain (which can affect the quality of the images), different T1 and T2 relaxation time, etc. Additionally, research should be done on other techniques that have been linked to HIE in the past, such as functional MRI and DTI. The revelation of a connection between these techniques and QSM will help to select the best method in terms of reliability, reproducibility, speed, and efficiency and push the boundaries of our understanding of HIE.

REFERENCES

1. Haacke, E.M., et al., *Quantitative susceptibility mapping: current status and future directions.* Magnetic resonance imaging, 2015. **33**(1): p. 1-25.
2. Weisskoff, R.M. and S. Kiihne, *MRI susceptometry: image‐based measurement of absolute susceptibility of MR contrast agents and human blood.* Magnetic resonance in medicine, 1992. **24**(2): p. 375-383.
3. Kurinczuk, J.J., M. White-Koning, and N. Badawi, *Epidemiology of neonatal encephalopathy and hypoxic–ischaemic encephalopathy*. Early human development, 2010. **86**(6): p. 329-338.
4. Bryce, J., et al., *WHO estimates of the causes of death in children.* The lancet, 2005. **365**(9465): p. 1147-1152.
5. Shankaran, S. and A.R. Laptook, *Hypothermia as a treatment for birth asphyxia.* Clinical obstetrics and gynecology, 2007. **50**(3): p. 624-635.
6. Golubnitschaja, O., et al., *Birth asphyxia as the major complication in newborns: moving towards improved individual outcomes by prediction, targeted prevention and tailored medical care.* EPMA Journal, 2011. **2**(2): p. 197-210.
7. van Beest, P., et al., *Clinical review: use of venous oxygen saturations as a goal-a yet unfinished puzzle.* Critical Care, 2011. **15**(5): p. 1-9.
8. Rescoe, E., et al., *Cerebral near-infrared spectroscopy insensitively detects low cerebral venous oxygen saturations after stage 1 palliation.* The Journal of thoracic and cardiovascular surgery, 2017. **154**(3): p. 1056-1062.
9. Liang, Z.-P. and P.C. Lauterbur, *Principles of magnetic resonance imaging: a signal processing perspective*. 2000: "The" Institute of Electrical and Electronics Engineers Press.
10. Nishimura, D.G., *Principles of magnetic resonance imaging*. 1996: Stanford University.
11. C.Westbrook, C.K.R., and J.Talbot *MRI in Practice.* Wiley-Blackwell, Ed UK: Blackwell Publishing Ltd, 2011(4th ed).
12. Gracien, R.-M., et al., *How stable is quantitative MRI?–Assessment of intra-and inter-scanner-model reproducibility using identical acquisition sequences and data analysis programs.* NeuroImage, 2020. **207**: p. 116364.
13. Schweser, F., et al., *Quantitative imaging of intrinsic magnetic tissue properties using MRI signal phase: an approach to in vivo brain iron metabolism?* Neuroimage, 2011. **54**(4): p. 2789-2807.
14. Liu, C., et al., *Quantitative susceptibility mapping: contrast mechanisms and clinical applications.* Tomography, 2015. **1**(1): p. 3-17.
15. Robinson, S.D., et al., *An illustrated comparison of processing methods for MR phase imaging and QSM: combining array coil signals and phase unwrapping.* NMR in Biomedicine, 2017. **30**(4): p. e3601.

16. Sun, H., et al., *Extracting more for less: multi‐echo MP2RAGE for simultaneous T1‐weighted imaging, T1 mapping, mapping, SWI, and QSM from a single acquisition.* Magnetic resonance in medicine, 2020. **83**(4): p. 1178-1191.

17. Gharabaghi, S., et al., *Multi-echo quantitative susceptibility mapping for strategically acquired gradient echo (STAGE) imaging.* Frontiers in neuroscience, 2020. **14**: p. 581474.

18. Smith, S.M., et al., *Advances in functional and structural MR image analysis and implementation as FSL.* Neuroimage, 2004. **23**: p. S208-S219.

19. Smith, S.M., *Fast robust automated brain extraction.* Human brain mapping, 2002. **17**(3): p. 143-155.

20. Ghiglia, D.C. and M.D. Pritt, *Two-dimensional phase unwrapping: theory, algorithms, and software.* A Wiley Interscience Publication, 1998.

21. Arevalillo-Herráez, M., M.A. Gdeisat, and D.R. Burton, *Hybrid robust and fast algorithm for three-dimensional phase unwrapping.* Applied optics, 2009. **48**(32): p. 6313-6323.

22. Baldi, A., *Phase unwrapping by region growing.* Applied optics, 2003. **42**(14): p. 2498-2505.

23. Schofield, M.A. and Y. Zhu, *Fast phase unwrapping algorithm for interferometric applications.* Optics letters, 2003. **28**(14): p. 1194-1196.

24. Peng, X., Z. Yang, and H. Niu, *Multi-resolution reconstruction of 3-D image with modified temporal unwrapping algorithm.* Optics communications, 2003. **224**(1-3): p. 35-44.

25. Schweser, F., A. Deistung, and J.R. Reichenbach, *Foundations of MRI phase imaging and processing for Quantitative Susceptibility Mapping (QSM).* Zeitschrift für medizinische Physik, 2016. **26**(1): p. 6-34.

26. Robinson, S., H. Schödl, and S. Trattnig, *A method for unwrapping highly wrapped multi‐echo phase images at very high field: UMPIRE.* Magnetic resonance in medicine, 2014. **72**(1): p. 80-92.

27. Zhao, M., et al., *Quality-guided phase unwrapping technique: comparison of quality maps and guiding strategies.* Applied optics, 2011. **50**(33): p. 6214-6224.

28. Abdul-Rahman, H.S., et al., *Fast and robust three-dimensional best path phase unwrapping algorithm.* Applied optics, 2007. **46**(26): p. 6623-6635.

29. Feng, W., J. Neelavalli, and E.M. Haacke, *Catalytic multiecho phase unwrapping scheme (CAMPUS) in multiecho gradient echo imaging: removing phase wraps on a voxel‐by‐voxel basis.* Magnetic resonance in medicine, 2013. **70**(1): p. 117-126.

30. Schweser, F., et al., *An illustrated comparison of processing methods for phase MRI and QSM: removal of background field contributions from sources outside the region of interest.* NMR in Biomedicine, 2017. **30**(4): p. e3604.

31. Shmueli, K., et al., *Magnetic susceptibility mapping of brain tissue in vivo using MRI phase data.* Magnetic Resonance in Medicine: An Official Journal of the International Society for Magnetic Resonance in Medicine, 2009. **62**(6): p. 1510-1522.

32. Liu, T., et al., *A novel background field removal method for MRI using projection onto dipole fields.* NMR in Biomedicine, 2011. **24**(9): p. 1129-1136.

33. Zhou, D., et al., *Background field removal by solving the Laplacian boundary value problem.* NMR in Biomedicine, 2014. **27**(3): p. 312-319.

34. Kressler, B., et al., *Nonlinear regularization for per voxel estimation of magnetic susceptibility distributions from MRI field maps.* IEEE transactions on medical imaging, 2009. **29**(2): p. 273-281.

35. Sun, H. and A.H. Wilman, *Background field removal using spherical mean value filtering and Tikhonov regularization.* Magnetic resonance in medicine, 2014. **71**(3): p. 1151-1157.

36. Li, W., B. Wu, and C. Liu, *Quantitative susceptibility mapping of human brain reflects spatial variation in tissue composition.* Neuroimage, 2011. **55**(4): p. 1645-1656.

37. Liu, T., et al., *Calculation of susceptibility through multiple orientation sampling (COSMOS): a method for conditioning the inverse problem from measured magnetic field map to susceptibility source image in MRI.* Magnetic Resonance in Medicine: An Official Journal of the International Society for Magnetic Resonance in Medicine, 2009. **61**(1): p. 196-204.

38. Wharton, S., A. Schäfer, and R. Bowtell, *Susceptibility mapping in the human brain using threshold‐based k‐space division.* Magnetic resonance in medicine, 2010. **63**(5): p. 1292-1304.

39. Wang, Y. and T. Liu, *Quantitative susceptibility mapping (QSM): decoding MRI data for a tissue magnetic biomarker.* Magnetic resonance in medicine, 2015. **73**(1): p. 82-101.

40. Sun, H., et al., *Whole head quantitative susceptibility mapping using a least-norm direct dipole inversion method.* Neuroimage, 2018. **179**: p. 166-175.

41. Blomgren, P. and T.F. Chan, *Color TV: total variation methods for restoration of vector-valued images.* IEEE transactions on image processing, 1998. **7**(3): p. 304-309.

42. Liu, J., et al., *Morphology enabled dipole inversion for quantitative susceptibility mapping using structural consistency between the magnitude image and the susceptibility map.* Neuroimage, 2012. **59**(3): p. 2560-2568.

43. Thukral, B.B., *Problems and preferences in pediatric imaging.* Indian Journal of Radiology and Imaging, 2015. **25**(04): p. 359-364.

44. Arthurs, O.J., et al., *The challenges of neonatal magnetic resonance imaging.* Pediatric radiology, 2012. **42**: p. 1183-1194.

45. Godenschweger, F., et al., *Motion correction in MRI of the brain.* Physics in medicine & biology, 2016. **61**(5): p. R32.

46. Hirokawa, Y., et al., *MRI artifact reduction and quality improvement in the upper abdomen with PROPELLER and prospective acquisition correction (PACE) technique.* American Journal of Roentgenology, 2008. **191**(4): p. 1154-1158.

47. Slipsager, J.M., et al., *Comparison of prospective and retrospective motion correction in 3D‐encoded neuroanatomical MRI.* Magnetic Resonance in Medicine, 2022. **87**(2): p. 629-645.

48. Blamire, A., *The technology of MRI—the next 10 years?* The British journal of radiology, 2008. **81**(968): p. 601-617.

49. Dias, S.C. and Ø.E. Olsen, *Isotropic 3-D T2-weighted spin-echo for abdominal and pelvic MRI in children.* Pediatric radiology, 2012. **42**: p. 1385-1390.

50. Liauw, L., et al., *Hypoxic-ischemic encephalopathy: diagnostic value of conventional MR imaging pulse sequences in term-born neonates.* Radiology, 2008. **247**(1): p. 204-212.

51. Chen, Y., et al., *Comparison of quantitative susceptibility mapping methods on evaluating radiation‐induced cerebral microbleeds and basal ganglia at 3T and 7T.* NMR in Biomedicine, 2022. **35**(5): p. e4666.

52. Li, T.Q., et al., *Characterization of T2* heterogeneity in human brain white matter.* Magnetic Resonance in Medicine: An Official Journal of the International Society for Magnetic Resonance in Medicine, 2009. **62**(6): p. 1652-1657.

53. Fang, J., et al., *Background field removal using a region adaptive kernel for quantitative susceptibility mapping of human brain.* Journal of Magnetic Resonance, 2017. **281**: p. 130-140.

54. Zhu, X., et al., *BFRnet: A deep learning-based MR background field removal method for QSM of the brain containing significant pathological susceptibility sources.* arXiv preprint arXiv:2204.02760, 2022.

55. Zhang, Y., et al., *Neonate and infant brain development from birth to 2 years assessed using MRI-based quantitative susceptibility mapping.* Neuroimage, 2019. **185**: p. 349-360.

56. Chai, C., et al., *Decreased susceptibility of major veins in mild traumatic brain injury is correlated with post-concussive symptoms: a quantitative susceptibility mapping study.* Neuroimage: clinical, 2017. **15**: p. 625-632.

(A)

APPENDIX A

Mean susceptibility values (x 10^{-3})

Method	ISMV	PDF	LBV	RESHARP	VSHARP	SHARP	MEAN
Hippocampus	-11.1	2.4	-18.8	-3.2	-6.7	-8.2	-7.6
Amygdala	-12.2	0.9	-24.2	-4.4	-6.6	-5.0	-8.6
Brainstem	-26.4	-9.2	-31.9	-14.8	-15.8	-18.3	-19.4
Caudate nucleus	2.8	-4.8	87	-1.0	0.2	-0.5	0.9
Thalamus	-7.1	-5.9	-2.2	-5.6	-5.0	-7.2	-5.5
Subthalamus nucleus	-17.6	-5.5	-18.3	-11.4	-18.8	-18.9	-15.1
Lentiform nucleus	-3.9	-0.1	-0.8	-3.2	-5.0	-5.2	-3.1
Corpus callosum	17.1	1.5	23.8	10.2	16	13.4	13.7
Lateral ventricle	14	8.4	17.9	12.0	14.6	12.4	13.2
Insula	-5.7	-2.7	-4.3	-5.9	-8.1	-6.8	-5.6
CSF	17	17.1	13.2	18.5	30.8	27.0	20.6
Deep fray matter	-3.3	-3.0	0.3	-3.1	-2.2	-3.5	-2.5
White matter	-1.6	-2.0	-4.3	-2.0	0.3	-0.5	-1.7
Cerebellum	-23.4	0.1	-41.3	-9.3	-6.7	-9.2	-15.0

(B)

Mean susceptibility values (x 10^{-3})								
Method	**NDI**	**MEDI**	**TIKH**	**TV**	**TKD**	**SSTGV**	**TSVD**	**MEAN**
Hippocampus	0.5	2.5	4.4	1.9	-0.4	-3.2	-3.6	0.3
Amygdala	-2.3	1.1	4.2	0.6	-1.9	-4.4	-5.4	-1.2
Brainstem	-15.4	-16.5	-14.1	-16.3	-15.2	-14.8	-13.9	-15.2
Caudate nucleus	1.2	1.6	4.1	1.5	0.3	-1.0	-1.4	0.9
Thalamus	-4.3	-4.4	-2.6	-4.0	-4.4	-5.6	-5.5	-4.4
Subthalamus nucleus	-10.2	-10.3	-7.3	-10.0	-10.9	-11.4	-12.1	-10.3
Lentiform nucleus	-1.3	0.2	2.3	-0.1	-1.6	-3.2	-3.8	-1.1
Corpus callosum	10.0	14.6	16.9	16.2	12.9	10.2	10.5	13.0
Lateral ventricle	13.4	17.8	17.7	18.8	14.8	12.0	10.8	15.1
Insula	-5.2	-6.2	-4.0	-5.1	-6.5	-5.9	-6.3	-5.6
CSF	21.5	25.2	23.9	24.8	21.3	18.5	16.6	21.7
Deep fray matter	-1.8	-1.2	0.9	-0.8	-1.9	-3.1	-3.2	-1.6
White matter	-0.1	-1.3	-0.9	-1.5	-1.8	-2.0	-1.9	-1.3
Cerebellum	-9.7	-10.8	-12.0	-10.1	-10.1	-9.3	-9.0	-10.2

Table 2: Mean susceptibility values for 14 different parts of the brain across the entire cohort when varying. (A) the dipole inversion methods with a fixed background field removal method (RESHARP) and (B) the background field removal for a fixed dipole inversion method (RTS).